Rayleigh invariance allows the estimation of effective CO_2 fluxes due to convective dissolution into water-filled fractures

Keim, Leon [1], **Class, Holger** [1]

[1]Institute for Modelling Hydraulic and Environmental Systems (IWS), University of Stuttgart

Key Points:

- Convective mixing of CO_2 in water-filled fractures shows 3-D effects and cannot be described with porous-media Darcy-models.
- Non-dimensionalization reduces the parameter space for estimating effective CO_2 flux rates due to convective dissolution.
- Fully developed fingering regimes after a certain time and fracture length reveal a Rayleigh invariance of the effective CO_2 fluxes.

Corresponding author: Keim, Leon, leon.keim@iws.uni-stuttgart.de

Abstract

Convective dissolution of CO_2 is a well-known mechanism in geological storage of CO_2. It is triggered by gravitational instability which leads to the onset of free convection. The phenomenon is well studied in porous media, such as saline aquifers, and the literature provides substantial evidence that onset times and effective flux rates can be estimated based on a characterization of instabilities that uses the Darcy velocity.

This work extends the study of convective dissolution to open water-filled fractures, where non-Darcy regimes govern the induced flow processes. Numerical simulations using a Navier-Stokes model with fluid density dependent on dissolved CO_2 concentration were used to compute scenario-specific results for effective CO_2 entry rates into an idealized fracture with varying aperture, temperature, and CO_2 concentration at the gas-water interface. The results were analyzed in terms of dimensionless quantities. They revealed a Rayleigh invariance of the effective CO_2 flux after the complete formation of a quasi-stationary velocity profile, i.e. after a certain entry length. Hence, this invariance can be exploited to estimate the effective CO_2 entry rates, which can then be used, in perspective, in upscaled models.

We have studied convective CO_2 dissolution for two different fracture settings; the first one relates to karstification scenarios, where CO_2 is the dominant driving force, and were stagnant-water conditions in fractures have not yet received attention to date. The second setting is inspired from geological CO_2 storage, where the literature provides only studies on convective CO_2 dissolution for porous-media flow with Darcy regimes.

Plain Language Summary

Carbon dioxide (CO_2) dissolves into water when the latter is in contact with a gaseous, CO_2-rich atmosphere. This process is characteristic for karst systems, where CO_2 originating from microbial activity in the soil is enriched in the atmosphere of caves or karstic void spaces. It is furthermore an important storage mechanism for CO_2 in deep geological reservoirs where the greenhouse gas is injected for mitigating global warming. When water is stagnant or without significant base flow, the dissolution process is governed by so-called convective dissolution, where convection cells are triggered by instabilities in the water body due to density differences caused by dissolved CO_2.

Convective dissolution is well understood, but it is still challenging to predict how much CO_2 dissolves over time. While literature studies on convective dissolution have been focused on porous rocks, we investigate here open fractures, where flow patterns are much more complex.

Using computationally expensive numerical simulations, we created a data basis for developing an approach to estimate effective CO_2 entry rates. A crucial finding is that these rates are invariant to a key dimensionless number, the Rayleigh number, which in this case describes the instability of a water body due to CO_2 dissolution.

1 Introduction

1.1 Motivation

Density-driven dissolution of CO_2 is a well-known process in geological storage of CO_2 (or: CCS - Carbon Capture and Storage). The literature refers to it also as convective mixing or convective dissolution. Related to CCS, convective dissolution is acknowledged to be an important storage mechanism, in this context also referred to as solubility trapping (Metz & Intergovernmental Panel on Climate Change, 2005). CO_2, accumulating in a supercritical fluid phase underneath a caprock of a geological storage reservoir, gradually dissolves in the resident brine and increases the brine's density (e.g.,

Garcia (2001)). The result is an unstable layering which can onset a process of fingering of CO_2-enriched brine, thus leading to an enhanced dissolution and an effective transport of CO_2. CCS has gained recognition for its capability to mitigate the adverse effects of climate change, with widespread research affirming its significance (Ipcc, 2022; Metz & Intergovernmental Panel on Climate Change, 2005; Kelemen et al., 2019; Boot-Handford et al., 2014; Scheer et al., 2021). Many studies have addressed convective dissolution, thereby considering the rock as a porous medium (Class et al., 2009; Bachu et al., 2007; Elenius & Johannsen, 2012; Kopp et al., 2009; Ennis-King, 2005; Flemisch et al., 2023; J. Nordbotten et al., 2012; Neufeld et al., 2010; Hesse, 2008). Some authors derived effective quantities for CO_2 fluxes by nondimensionalization and the usage of characteristic quantities such as the Darcy velocity as characteristic velocity, e.g. (Ennis-King, 2005; Hesse, 2008).

Beyond the assumption of Darcy flow, there is literature available in the field of thermal natural convection, e.g., (Grossmann & Lohse, 2000, 2001) . There are, however, notable differences between thermal convection and convection induced by CO_2 concentrations, such that the scaling laws cannot be easily transferred. Viscosity is much stronger affected by temperature than it is dependent on CO_2 concentrations. In the thermal-convection field, some studies focus on turbulent convection (Ahlers & Xu, 2001; Grossmann & Lohse, 2004), which is not the case for CO_2-induced convection. Thermal-convection studies are reported for 2-D domains, where lateral influences of boundary-layer development are studied (Ahlers et al., 2009). Regarding convective flow in fractures, it is rather important to consider the boundary-layer development in a fracture plane, i.e. in the void space defined by the aperture.

To the best of our knowledge, the literature has not extended so far the study of convective dissolution of CO_2 to fractured media, where permeabilities are significantly larger, and where Darcy-regimes are not given anymore. In such cases, the hydraulic characteristics are distinctly different from porous-media systems, even for fractures as narrow as 1 mm (De Paoli et al., 2020). We have shown previously in a water-filled fracture with 1 cm aperture that onset time of fingering and fingering patterns cannot be matched with approaches that are valid in porous-media systems (Class et al., 2020).

Within the scope of CCS, the presence of small fractures introduces numerous challenges. Fractured caprock could act as a pathway for CO_2 leakage. A significant body of research has been devoted to understanding the implications of such fractures (J. A. White et al., 2014; Song & Zhang, 2013; Rutqvist et al., 2008; Ellis et al., 2011; Hommel et al., 2020; Fernø et al., 2023). Our focus, however, lies on fractures that may exist underneath the caprock similar to March et al. (2018). A research question in this regard may be if permeable fractures can foster the onset of fingering regimes in geological reservoirs and thereby enhance or accelerate the solubility trapping of CO_2.

Convective dissolution of CO_2 can also play an important role in karstic systems (Class et al., 2021, 2023). Karst plays a pivotal role in the global carbon cycle, with karstic springs releasing huge amounts of CO_2 to the atmosphere (Lee et al., 2021), which might even make them potentially interesting as sites for carbon capture. A significant share of the CO_2 released at karstic springs has long before entered the karstic system through complex interacting processes at the epiphreatic interface between vadose zone and saturated zone and is then driving karstification and speleogenesis (Audra & Palmer, 2011; Kaufmann et al., 2014; Bakalowicz, 2005; Riechelmann et al., 2019; Klimchouk et al., 2000; Houillon et al., 2020). Speleogenesis, the study of cave formation, considers compositional water and gas flow as well as thermal processes and not only captivates a broad scientific audience but also carries implications for the construction and maintenance of infrastructure in karstic regions and the exploration of geothermal resources (Luetscher & Jeannin, 2004) Karstic systems are characteristically dominated by fissures, fractures, and large void spaces, where during periods of stagnant water, density-driven enhanced dissolution of CO_2 at the epiphreatic interface can contribute new limestone-dissolutional

power; this has not yet received attention in karst literature (Class et al., 2021). CO_2 concentrations in the vadose air of karstic systems are typically highly elevated relative to atmospheric values, for example up to levels of 1-2 % in the Swabian Jura (South Germany) (Class et al., 2023) and strongly dependent on the season and corresponding ventilation patterns (Kukuljan et al., 2021).

Traditional theories of speleogenesis have solely relied on flowing water streams (Bögli, 1980; Gabrovšek & Dreybrodt, 2000; Dreybrodt, 1988), while recent insights suggest that density-driven CO_2 dissolution into stagnant water can also be a significant factor (Class et al., 2021) under certain conditions. Intermittent stagnant water conditions occur during dry periods and in confined spaces such as fractures and fissures. Seasonal gaseous CO_2 transfer through the epikarst, from the uppermost soil layer into the water bodies below, is a potential pathway for CO_2 and can lead to periods, where the gaseous CO_2 is not in equilibrium with the dissolved CO_2 at the karstwater table (Class et al., 2023; Covington, 2016). For that reason, convective dissolution of CO_2 into karst fractures is a mechanism of interest and needs to be quantified. An improved understanding will allow for a potentially required adaption of karstification theories and limestone dissolution models.

1.2 Estimating Effective Fluxes in Porous-Media Systems

Research on porous media has made significant progress in predicting the characteristics of CO_2 fluxes due to convective mixing, particularly focusing on two key aspects: (i) the onset times of convective-mixing and (ii) the effective flux during a developed constant-flux regime. Central to these investigations is the utilization of porous-media models, where Darcy's law is predominantly used to model fluid flow. This foundational approach forms the basis for much of the theoretical and computational modeling in the field. For an overview it is referred to (Emami-Meybodi et al., 2015).

Some authors introduced a flux efficiency $\langle F \rangle$ [-], which is related to the dimensional flux of CO_2 from the gas phase into the aqueous phase, F [kg/(m^{2}s)] (or [mol/(m^{2}s)]), as expressed by

$$F = \langle F \rangle u_c \rho x_{\mathrm{CO_2},c}\,, \tag{1}$$

where u_c [m/s] represents a characteristic velocity and x_c is a mass (or mole) fraction of the CO_2 in the aqueous phase at the interface with the gas phase. In the context of porous media, u_c is the Darcy velocity, which is commonly calculated based on the characteristic density difference between the brine with a CO_2 concentration of x_c and a pure brine. One could interpret this as a scaling to a characteristic advective, buoyant flux. Since u_c is known a-priori, a sound understanding of $\langle F \rangle$ yields a prediction of the dimensional flux rates during convective mixing.

Many studies have investigated $\langle F \rangle$. In this paper, the notion is used from De Paoli et al. (2020), while others use also $\langle \frac{dC}{d\tau} \rangle$ (Hesse, 2008), χ (Kneafsey & Pruess, 2010) or $\langle \epsilon \rangle$ (Hidalgo et al., 2012), or refer to it just as flux (dimensionless) (Green & Ennis-King, 2018). The value of $\langle F \rangle$ during a constant flux-regime has been determined in numerical simulations and is reported as 0.017 (Hesse, 2008; Green & Ennis-King, 2018), 0.0120 (neglecting the weak Rayleigh dependence), or 0.02 (Elenius & Johannsen, 2012).

In De Paoli et al. (2020), non-Darcy effects in a fluid-filled Hele-Shaw cell, which can also be interpreted as a fluid-filled fracture, were investigated. Those authors found that the classification of Letelier et al. (2019), using the product ϵ^2 Ra with ϵ being the cell anisotropy ratio $\epsilon = \sqrt{k}/H = \sqrt{(a^2/12)}/H$ and the Darcy Rayleigh number Ra as criterion, clearly distinguished three characteristic regimes in the experimental results from De Paoli et al. (2020), i.e., the Darcy regime, the Hele-Shaw regime and the 3-D regime. For their experiment with apertures of 0.8 and 1 mm (ϵ^2 Ra $>> 1$), both rep-

resenting the 3-D regime, $\langle F \rangle$ is significantly lower compared to Darcy-regime experiments.

Since one of the aims of this study is to predict the flux for the range of regimes from Darcy regime to 3-D regime, fractures and fissures in karstic systems reaching apertures of several centimeters pose a challenge. The commonly applied assumption that the parallel-plate flow model can be used to translate a fracture aperture into a permeability for Darcy's law, i.e. $k = \frac{a^2}{12}$, is not valid under these conditions. Thus, choosing the characteristic velocity to be a Darcy estimate is not expedient. Instead, the idea is to determine the finger-front velocity individually by numerical simulations and to apply this characteristic velocity for all fracture scenarios of our interest. To tackle the problem of predicting fluxes in fractures with large apertures, the suggestion of De Paoli et al. (2020) to investigate the matter using 3-D Navier-Stokes simulations is followed in this study. However, for deriving effective quantities and flux predictions, the findings and approaches in porous-media research are kept in mind and used as references.

To our knowledge, there is no study investigating the transition from the Darcy regime to the 3-D regime using 3-D Navier-Stokes equations.

1.3 Aims and Outline of this Study

This study aims at extending the estimation of effective CO_2 fluxes due to convective dissolution to non-Darcy regimes in water-filled fractures. The focus of application is twofold and includes both karstic systems and geological CO_2 storage systems.

These two fields of application show common features but also distinct differences. Both are associated with typical subsurface uncertainties regarding the details of properties like porosity and permeability, and, more relevant here, regarding the distribution and geometries of fractures, fissures, and small void spaces. Considering further the huge challenges regarding the computational demands for spatially and temporally highly resolved numerical simulations, it is obvious that field-scale models will require effective upscaled quantities rather than fully-resolved physics.

The dynamics of natural convection processes are favored by high driving forces and low resistance to these forces. Employing this to the two fields of application, this means that both the driving forces and the resistance to them are smaller in karst than in CO_2 storage geological reservoirs. CO_2 gas-phase concentrations in karst systems are realistic in a range of 1-2 %, while the brine in contact with supercritical CO_2 in a storage reservoir is at saturated CO_2 concentration. On the other hand, karstic fissures and fractures are highly variable up to several centimeters aperture, while we consider rather a range of up to a few millimeters to be realistic in CCS-related fractured systems.

We want to find out how effective quantities for CO_2 fluxes can be determined and derived from highly resolved numerical simulations in an idealized fracture of varying aperture and height, while being exposed to different CO_2 concentrations at the top to represent realistic karst settings on the one hand and CCS-related settings on the other hand. We want to investigate whether the methodology is robust in both ends of the spectrum, i.e. for larger apertures and lower CO_2 concentrations as it is characteristic for karst, and for smaller apertures and high CO_2 concentrations as in CCS-type systems. By deriving these quantities, we aim at approximating the vertical fluxes due to convective mixing, while, in perspective, enabling simulations on a larger scale. Towards achieving this aim, we will further predict the necessary velocity scales under typical conditions for both karstic and CCS environments.

This article is structured as follows: Section 2 provides the theoretical background with the basic assumptions, conceptual ideas, and methods of the study as well as the governing equations. After that, in Section 3, the details regarding the numerical sim-

ulations are given; we refer to these numerical simulations also as the numerical experiments, since they provide the basis for the interpretation, analysis, and discussion of the results in Section 4. The article closes with the basic conclusions from this study.

2 Theory

A fundamental relevance of this study arises in convective dissolution processes, where 3-D effects play a role, which ultimately affect the efficiency of CO_2 influx into water-filled fractures. This may occur in karst systems or also in geological storage scenarios. Thereby, the CO_2 concentrations, the temperatures, the apertures of the fractures and their roughnesses, their inclinations, connectivity, etc. can be very different and many of these quantities are inherently very variable. For this reason, we consider it necessary and opportune to use a generic single-fracture scenario for this study, which may serve as the basis for an upscaling to field-scale application. First of all, the underlying assumptions of the study are introduced; then the basic model equations are explained, followed by the non-dimensionalization of the model variables. At the end of this 'Theory section', the influence of boundary-layer development on the formation of a fully developed velocity profile in a single fracture is explained.

2.1 Assumptions and Approach

While other studies conceptualise a fracture as a lower-dimensional porous medium (Berre et al., 2021; Flemisch et al., 2018; J. M. Nordbotten et al., 2019), this study aims at explicitly demonstrating effects which occur for fractures where assumptions of porous-media flow (Darcy flow) are not valid. A schematic representation of a fracture as it is used for the numerical simulations in this study can be seen in Figure 1. The water-filled fracture is exposed to a given concentration gas-phase concentration of CO_2 at the top, which translates into a concentration of dissolved CO_2 in the aqueous phase, serving as a Dirichlet boundary condition at the top boundary. For scenarios where the resistance to induced convective flow is overcome, a fingering regime will be triggered after some time, and we can determine a finger-front velocity, which will in the further serve as a characteristic velocity for non-dimensionalization.

In order to evaluate the finger-front velocity, different control heights are employed to track breakthrough curves. A control height is a certain vertical distance measured from the bottom of the conceptual fracture as seen in Figure 1. The calculated concentrations of each cell, intersected by the horizontal plane at a given control-height, are continuously stored in the numerical simulation runs. In a post-processing step, these values are used to determine breakthrough times and, related to the respective distance between control-heights, a depth-dependent finger-front velocity. Note that, control heights are inverse to the depth; i.e., the control-height of 0 would represent the bottom of the fracture, while the depth of 0 would represent the top boundary.

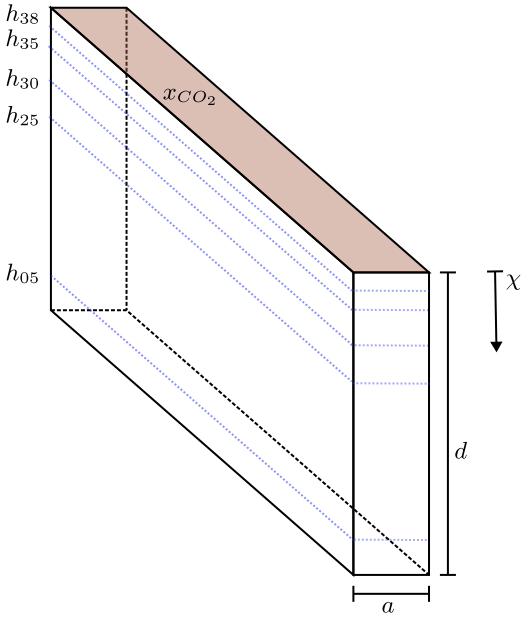

Figure 1: Conceptual fracture representation: A constant concentration of CO_2 is imposed at the top boundary. The lower-boundary is no-flow. Front and back faces are non-slip boundaries, while left and right boundaries (here the viewer-facing boundaries) are periodic. Control heights to evaluate breakthroughs are denoted with h and their respective height (in [cm]). The depth of the fracture is denoted with d. h is measured from the bottom while the depth is measured from the gas-water interface. The aperture is denoted with a. χ represents a variable to parameterize depth.

Further conceptual assumptions are the following:

- The generic fracture is conceptualized as a cuboid and the dimension in the direction of the aperture is discretized.
- Wall roughness of the fractures is neglected.
- It is assumed that the fracture is water-filled. This implies that the primary fluid within the void space of the fracture is water, and no other phase is present in its interior. Furthermore, the diffusion is modelled by using an approach for molecular diffusion in the aqueous phase. For karstic systems, this assumption is rather standard and allows even for large void spaces such as conduits (Hartmann et al., 2014). For CCS-systems, fractures with an aperture of up to 1 mm have been reported (Iding & Ringrose, 2010).
- Aquatic chemistry is not taken into account. In particular this assumption is recommended to study in future research, since the concentration of dissolved carbon in water is significantly influenced by the pH level, and further chemical reactions happen at the interface between water and the rock-matrix (Pankow, James F., 2022; Appelo & Postma, 2010; W. M. White, 2013).

2.2 Governing Equations

For the numerical simulations, we solve the following set of equations.

262 ***Conservation of Momentum***

Dependent on the properties of the individual fracture scenario and the corresponding flow regime, basically three equations can be considered for the conservation of momentum. In De Paoli et al. (2020), a definition of three characteristic regimes is given. For fractures of aperture size << 1 mm, a quasi-Darcy approach with a parallel-plate model is possible, with the permeability calculated from the fracture aperture as

$$k = \frac{a^2}{12}\,. \tag{2}$$

The equation for the momentum conservation is then expressed using Darcy's law.

$$\mathbf{u} = -\frac{k}{\mu}\left(\nabla p + \rho \mathbf{g}\right) \tag{3}$$

For fractures of apertures >> 1 mm, the conservation of momentum is modelled using the 3-D Navier-Stokes equations and the Boussinesq approximation, $(.)_0$ refers to the initial state.

$$\frac{\partial \mathbf{u}}{\partial t} + (\mathbf{u}\cdot\nabla)\mathbf{u} = -\frac{1}{\rho_0}\nabla(p - \rho_0 \mathbf{g}\cdot\mathbf{z}) + \nu\nabla^2\mathbf{u} - \mathbf{g}\gamma(x_{\mathrm{CO_2}} - x_{\mathrm{CO_2},0}) \tag{4}$$

where:

$$\gamma = -\left(\frac{1}{\rho}\frac{\partial \rho}{\partial x_{\mathrm{CO_2}}}\right)\Bigg|_0 \tag{5}$$

263 In between those clearly distinguished regions, there is a region where a quasi-3D,
264 i.e. effectively a 2-D Navier-Stokes model is extended by a drag term to account for non-
265 slip conditions at the fracture walls (Class et al., 2020).

$$\frac{\partial \mathbf{u}}{\partial t} + (\mathbf{u}\cdot\nabla)\mathbf{u} = -\frac{1}{\rho_0}\nabla(p - \rho_0 \mathbf{g}\cdot\mathbf{z}) + \nu\nabla^2\mathbf{u} - \mathbf{g}\gamma(x_{\mathrm{CO_2}} - x_{\mathrm{CO_2},0}) - c\frac{\nu}{a^2}\mathbf{u}$$

266 ***Mass Conservation of the Aqueous Phase***

The conservation of mass of the phase is given by

$$\nabla\cdot\mathbf{u} = 0\,. \tag{6}$$

267 Changes in density are only considered in the momentum equation.

268 ***Mass Conservation of Dissolved CO_2***

The transport of CO_2 in the aqueous phase is described by

$$\frac{\partial x_{\mathrm{CO_2}}}{\partial t} + \nabla\cdot(\boldsymbol{u}\cdot x_{\mathrm{CO_2}} - D_{\mathrm{CO_2}}\cdot\nabla x_{\mathrm{CO_2}}) = 0\,. \tag{7}$$

269 **2.3 Non-dimensionalization and Dimensionless Numbers**

Derived effective quantities from the CCS-related literature heavily relied on non-dimensionalization and dimensionless numbers, most importantly the Rayleigh number (Ennis-King, 2005; Hesse, 2008), typically written in the following form:

$$Ra = \frac{k_z\, g\, \Delta\rho\, L_c}{\mu\, D}\,. \tag{8}$$

Darcy's law can be used to calculate a characteristic vertical velocity, u_c due to the characteristic driving force for the fingers, $\Delta\rho$, and the resistance to that in terms of viscous effects, dominated by the vertical permeability, k_z. Then, u_c is obtained as

$$u_c = \frac{k_z\, g\, \Delta\rho}{\mu} = \frac{a^2 \Delta\rho g}{12\mu} \tag{9}$$

and the Rayleigh number accordingly

$$Ra = \frac{u_c L_c}{D}\,, \tag{10}$$

which shows that this definition of Ra suggests in fact an interpretation as a Péclet number, i.e., convection versus diffusion. This definition also arises when Equation (7) is non-dimensionalized, using the standard approach that a dimensional quantity can be described with a characteristic dimensional quantity and a dimensionless quantity. For instance $t = t_c \cdot \widehat{t}$ where $(.)_c$ denotes the dimensional characteristic quantity and $\widehat{(.)}$ denotes the dimensionless quantity. Applying this procedure to Equation (7) yields similar to Hesse (2008):

$$\frac{x_{\mathrm{CO_2},c}}{t_c}\frac{\partial \widehat{x}_{CO_2}}{\partial \widehat{t}} + \frac{u_c x_{\mathrm{CO_2},c}}{L_c}\widehat{\nabla}\cdot\left(\widehat{\boldsymbol{u}}\cdot\widehat{x}_{CO_2}\right) - \frac{x_{\mathrm{CO_2},c}}{L_c^2}\widehat{\nabla}\cdot\left(D_{\mathrm{CO_2}}\cdot\widehat{\nabla}\widehat{x}_{CO_2}\right) = 0 \tag{11}$$

Choosing $t_c = L_c/u_c$ and dividing by $u_c x_{\mathrm{CO_2},c}/L_c$, results in:

$$\begin{aligned}\frac{\partial \hat{x}_{CO_2}}{\partial \hat{t}} + \hat{\nabla}\cdot\left(\hat{\boldsymbol{u}}\cdot\hat{x}_{CO_2} - \frac{D_{\mathrm{CO_2}}}{u_c L_c}\cdot\hat{\nabla}\hat{x}_{CO_2}\right) &= 0\\ \frac{\partial \hat{x}_{CO_2}}{\partial \hat{t}} + \hat{\nabla}\cdot\left(\hat{\boldsymbol{u}}\cdot\hat{x}_{CO_2} - \frac{1}{Ra}\cdot\hat{\nabla}\hat{x}_{CO_2}\right) &= 0\end{aligned} \tag{12}$$

The interpretation of the Rayleigh number in this study will follow the same understanding. During the fingering regime it is interpreted as the ratio between convective and diffusive fluxes of CO_2, exactly as the Péclet number is interpreted. Hence, it is hypothesized that if one can reliably estimate the characteristic velocity of the fingers, this should also allow for estimating the flux rate of CO_2 during the fingering regime.

Studies outside the field of porous media use a different definition of the Rayleigh number. It arises from non-dimensionalizing the Navier-Stokes equations, including the Boussinesq approximation. Expanding the vector notation of Equation (4) into each dimension and assuming that gravity acts in the y-direction results in the following set of equations:

$$\rho_0\left(\frac{\partial u}{\partial t} + \frac{\partial uu}{\partial x} + \frac{\partial vu}{\partial y} + \frac{\partial wu}{\partial z}\right) = -\frac{\partial p}{\partial x} + \mu\left(\frac{\partial^2 u}{\partial x^2} + \frac{\partial^2 u}{\partial y^2} + \frac{\partial^2 u}{\partial z^2}\right) \tag{13}$$

$$\begin{aligned}\rho_0\left(\frac{\partial v}{\partial t} + \frac{\partial uv}{\partial x} + \frac{\partial vv}{\partial y} + \frac{\partial wv}{\partial z}\right) =&\\ -\frac{\partial p + \rho_0 g y}{\partial y} + \mu\left(\frac{\partial^2 v}{\partial x^2} + \frac{\partial^2 v}{\partial y^2} + \frac{\partial^2 v}{\partial z^2}\right) &+ \rho_0 g \gamma \Delta x_{\mathrm{CO_2}}\end{aligned} \tag{14}$$

$$\rho_0\left(\frac{\partial w}{\partial t} + \frac{\partial uw}{\partial x} + \frac{\partial vw}{\partial y} + \frac{\partial ww}{\partial z}\right) = -\frac{\partial p}{\partial z} + \mu\left(\frac{\partial^2 w}{\partial x^2} + \frac{\partial^2 w}{\partial y^2} + \frac{\partial^2 w}{\partial z^2}\right) \tag{15}$$

The same procedure shown for the derivation of Equation (12) is used for the non-dimensionalisation of the momentum balance in the direction of gravity (here, Equation (14), for further details it is referred to Appendix A), yielding :

$$\begin{aligned}\frac{\partial \widehat{v}}{\partial \widehat{t}} + \frac{\partial \widehat{u}\widehat{v}}{\partial \widehat{x}} + \frac{\partial \widehat{v}\widehat{v}}{\partial \widehat{y}} + \frac{\partial \widehat{w}\widehat{v}}{\partial \widehat{z}} =&\\ \frac{\partial \widehat{p}}{\partial \widehat{y}} + \underbrace{\frac{\mu}{\rho_0 L_c v_c}}_{I}\left(\frac{\partial^2 \widehat{v}}{\partial \widehat{x}^2} + \frac{\partial^2 \widehat{v}}{\partial \widehat{y}^2} + \frac{\partial^2 \widehat{v}}{\partial \widehat{z}^2}\right) &+ \underbrace{\frac{g\gamma\Delta x_{\mathrm{CO_2}} L_c}{v_c^2}}_{II}\widehat{x}_{TIC}\end{aligned} \tag{16}$$

Choosing $u_c = D/L_c$, yields for the terms I and II:

$$\begin{aligned} I &: \frac{\mu}{\rho_0 L_c u_c} = \frac{\mu}{\rho_0 D} = \frac{\nu}{D} && = Sc \\ II &: \frac{g\gamma\Delta x_{\mathrm{CO_2}} L_c}{u_c^2} = \frac{g\gamma\Delta x_{\mathrm{CO_2}} L_c^3}{D^2} = \frac{g\rho_0\gamma\Delta x_{\mathrm{CO_2}} L_c^3}{D\mu}\frac{\nu}{D} && = Ra \cdot Sc \end{aligned} \tag{17}$$

This results in the following definition of the Rayleigh number:

$$Ra = \frac{g\Delta\rho L_c^3}{D\mu}\,. \tag{18}$$

In the derivation above, the definition of the Rayleigh number arises from the momentum equation and has a different physical meaning than the one used in the porous-media context. Regarding similitude, the two different approaches for the Rayleigh number are not straightforwardly transferable. We have shown above that there are three distinct regimes, i.e., the Darcy regime as the one extreme, the 3-D free-flow regime as the other extreme, and the transitioning between them. Accordingly, the momentum equation has to be chosen, and its corresponding non-dimensionalization results in the two different Rayleigh-number approaches. For this study, we choose to use the approach derived from porous-media (Darcy) context, while being well aware that this is not perfect for the entire range of flow regimes.

It is known from the above-referenced porous-media literature that this definition of the Rayleigh number resembling a Péclet number showed reliable results in the pursuit of deriving effective quantities. As already mentioned, we choose the finger-front velocity as the characteristic velocity, u_c.

2.4 Prandtl-Blasius Boundary Layer

The finger-front velocity is determined by monitoring breakthroughs of the CO_2 concentration at various depths, also referred to as control heights (see Figure 1). However, this approach of detecting breakthroughs poses another challenge. Dependent on apertures and velocities, the development of the Prandtl-Blasius boundary layer has different impacts. Commonly, the Prandtl-Blasius boundary layer for laminar flow is described in the following form:

$$\frac{\delta}{x} = \frac{5.0}{{Re_x}^{1/2}} \tag{19}$$

δ is the boundary layer thickness, while x is the distance from the origin of the boundary layer development into the direction of the flow. Accordingly, Re_x is obtained with x as the characteristic length. In the case of our idealized fracture (see Figure 1) during natural convection, there are two boundary layers evolving, i.e., one from each non-slip boundary. Furthermore, to avoid confusion, χ was introduced to represent the distance to the gas-water interface, i.e., to parameterize water depth. For a visualization see Figure 1. Hence, x in Equation (19) is χ in the following.

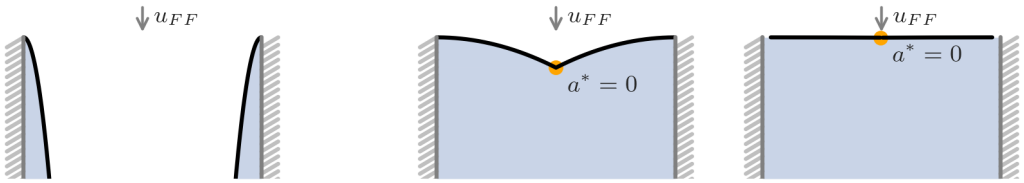

Figure 2: Development of the Prandtl-Blasius boundary layers visualized for the uppermost 10 cm. Apertures are from left to right: 1 m, 0.1 m, and 0.01 m. For u_{FF} a velocity of 1.8 cm/min. The profile will look different for different velocities.

Figure 2 shows the qualitative development of boundary layers in the schematic parallel-plate fracture; the boundary layers merge after a certain time and length into a fully developed flow profile in the cross section if the fracture has enough vertical depth relative to the given flow velocity, u_{FF}, and aperture, a. For small apertures and/or high velocities the two boundary layers tend to merge faster. It is, thus, evident that an evaluation of the finger-front velocity is dependent on the development of the boundary layer if the flow profile within the fractures is not yet fully developed. The boundary layer is caused by viscous effects that tend to slow down the finger-front velocity. Now recall that we intend to employ the finger-front velocity as a measure to relate eventually to the estimate of the CO_2 influx into the fracture by convective dissolution, i.e., we want to multiply the finger-front velocity with the cross-sectional area. Before the boundary layers merge, i.e. for higher control heights (see Figure 1), the finger-front velocity is not yet, or at least less affected by the boundary layer, while the cross-sectional area, where the total effective CO_2 flux occurs, is already affected by the viscous effects. In other words, there is no cross-sectional area defined solely by the aperture where CO_2 is transported with the proposed finger-front velocity. Yet, for obtaining flux as the product of cross-sectional area times finger-front velocity, a proper definition of the area is required, since the boundary layer affects how representative a finger-front velocity is for the entire cross section. This issue is more likely to be relevant for fractures occurring in karstic systems, since smaller fractures have a fully developed boundary layer almost immediately. To illustrate this, we refer to the exemplary fracture of Figure 2, where this would translate to 1 cm or smaller. It is therefore proposed to take into account how much of the fracture's cross-sectional area in a certain depth is not (yet) within the boundary layer. This is achieved by introducing a corrected aperture, $a^\star$:

$$a^\star = \begin{cases} 0, & \text{for } a \leq 2\delta \\ a - 2\delta, & \text{for } a > 2\delta \end{cases} \tag{20}$$

3 Numerical Simulations

Numerical simulations of convective dissolution scenarios in the schematic single fracture were carried out in order to generate the data for subsequent interpretation with regard to dimensionless quantities. This section provides information and explanations regarding the applied and adapted OpenFOAM simulator. The section further introduces the individual scenarios, which are categorized as (i) karstic and (ii) CCS. This categorization helps to link the scenarios to realistic fields of application and explains the range of values used for fracture apertures and CO_2 concentrations. We keep in mind that karstic systems typically have much lower CO_2 concentrations than CCS systems, while the apertures in karst are much higher than in geological reservoirs for CCS.

3.1 The OpenFOAM Simulator

In this study, the OpenFOAM (v22.12) computational fluid dynamics (CFD) toolkit was used to simulate fluid flow and solute transport, in particular the BoussinesqPimpleFoam solver. To improve the accuracy of the model and to ensure physical relevance, a convergence criterion based on the relative shift of the total moles was implemented. The code can be seen and run using a Docker image (Keim & Class, 2024a).

3.2 Computing Infrastructure

The Simulations were conducted on the Experimental Compute Cluster of the EXC 2075 Stuttgart Center for Simulation Science (SimTech), University of Stuttgart. The most resource-demanding simulation in our study was conducted on two fully occupied nodes. Each node consists of 128 cores (2x 64 core, AMD EPYC 7702) with 2 TB RAM. Simulating 320 s (simulated time) required 5 days computation time on the cluster. However, note that the load for a single-fracture simulation highly depends on the fracture

and it's respective mesh. Other simulation runs were much less demanding, being able to simulate 5,000 s on half a node in less than 5 days. Unfortunately, the smaller the aperture the higher the computational cost due to restrictions in the aspect ratio and a minimum amount of degrees of freedom in the direction of the aperture width.

3.3 Scenarios Related to Karstic Systems

To investigate the influence of open fractures in karstic systems, a coarse screening of the orders of magnitude was performed, i.e., concentrations ranged from 1×10^{-03} to 1×10^{-05} [mol/mol], while the aperture ranged from 1×10^{-03} m to 1×10^{-01} m. In a second step, a refined screening was carried out for a fracture of 1 cm in order to identify the concentration at which fingering does not initiate because of too much viscous resistance.

It is known that fractures with apertures significantly smaller than 1 mm can be represented using the Darcy approximation (De Paoli et al., 2020). It was decided that the smallest relevant fracture in this study is one with an aperture of 1 mm. As can be seen in Class et al. (2023), a seasonal variation in the aqueous CO_2 concentration of 1×10^{-04} [mol/mol] is common in the field. Therefore, this value was chosen as the reference for the karst-related systems of this study. 8 $°C$ is a typical temperature found, for example, in the caves of the Swabian Jura (southern Germany). However, we also simulated scenarios at 20 $°C$ to represent potential tropical karst systems. To our knowledge, there is no publicly available dataset describing seasonal CO_2 concentrations in tropical caves, so we decided to use the same representative values as found in the Swabian Jura. We note that assuming the same aqueous CO_2 concentration at different temperatures does not imply that the corresponding air CO_2 concentration is the same, due to the temperature dependence of the Henry coefficient.

A summary of all simulations conducted for the karstic systems can be found in Table 1

Table 1: Karst-related scenarios and chosen parameter variations

Scenario	**Temperature** $[^\circ C]$	**Aperture** [m]	**Concentration** $[\frac{\text{mol}}{\text{mol}}]$
I	8	1×10^{-3}	1×10^{-5}
II	8	1×10^{-3}	1×10^{-4}
III	8	1×10^{-3}	1×10^{-3}
IV	8	1×10^{-2}	1×10^{-5}
V	8	1×10^{-2}	8×10^{-6}
VI	8	1×10^{-2}	1×10^{-4}
VII	8	1×10^{-2}	2×10^{-5}
VIII	8	1×10^{-2}	1×10^{-3}
IX	8	1×10^{-1}	1×10^{-5}
X	8	1×10^{-1}	8×10^{-6}
XI	8	1×10^{-1}	1×10^{-4}
XII	8	1×10^{-1}	2×10^{-5}
XIII	8	1×10^{-1}	1×10^{-3}
XIV	20	1×10^{-3}	1×10^{-5}
XV	20	1×10^{-3}	1×10^{-4}
XVI	20	1×10^{-3}	1×10^{-3}
XVII	20	1×10^{-2}	1×10^{-5}
XVIII	20	1×10^{-2}	8×10^{-6}
XIX	20	1×10^{-2}	1×10^{-4}
XX	20	1×10^{-2}	2×10^{-5}
XXI	20	1×10^{-2}	1×10^{-3}
XXII	20	1×10^{-1}	1×10^{-5}
XXIII	20	1×10^{-1}	8×10^{-6}
XXIV	20	1×10^{-1}	1×10^{-4}
XXV	20	1×10^{-1}	2×10^{-5}
XXVI	20	1×10^{-1}	1×10^{-3}

3.4 Scenarios Related to CCS Systems

The other end of the range in terms of CO_2 concentrations is represented in the CCS-related scenarios, which were motivated by the scenarios investigated by Kopp et al. (2009). Since the concentration of CO_2 is governed by the solubility limit of CO_2 (determined after Duan and Sun (2003)), the conditions in terms of pressure and temperature are determined by the location and properties of the aquifer's environment. The letters D, C, and S represent, accordingly, a deep, cold, and shallow aquifer. The corresponding fluid properties are shown in Table 5. It was decided to only model a 1 mm fracture aperture, since everything beyond that seems rather unrealistic and everything far below can be modelled using porous-media equations.

Table 2: CCS-related scenarios and their parameter variations

Scenario	**Aperture** [m]	**Concentration** $[\frac{\text{mol}}{\text{mol}}]$
S	1×10^{-3}	0.034
C	1×10^{-3}	0.038
D	1×10^{-3}	0.039

3.5 Fluid Properties

Values of the fluid properties used in the karstic study are listed in Table 3 and are calculated using the following models; reference density (Wagner & Pruß, 2002; "IAPWS Industrial Formulation 1997 for the Thermodynamic Properties of Water and Steam", 2008), viscosity (Kestin et al., 1978), molecular diffusion coefficient of CO_2 (Unver & Himmelblau, 1964) and the γ-parameter to describe the density dependence of CO_2 is derived after Garcia (2001).

For the CCS scenarios the fluid propertires are summarized in Table 5. Due to the effects of salinity different consitutive relations are used; solubility of CO_2 (Duan & Sun, 2003); reference density (Yan et al., 2011; Phillips et al., 1981), viscosity ("IAPWS Industrial Formulation 1997 for the Thermodynamic Properties of Water and Steam", 2008; Phillips et al., 1981), molecular diffusion coefficient of CO_2 (Omrani et al., 2022) and the γ-parameter is again derived after Garcia (2001).

To derive γ, the reference state is equal to the initial condition of a simulation run i.e., a CO_2 concentration of zero. This is then used to calculate the fluid density at these reference conditions. After that, the fluid density is determined for an assumed occurrence of the peak CO_2 concentration within the system of interest. In the karstic setting, this is the aqueous CO_2 concentration in correspondence to a seasonally elevated gaseous CO_2 concentration inside a cave, or, in the CCS setting, it is the solubility of CO_2 under reservoir conditions. Finally, a linearization of the density values between the two determined points is conducted. The resulting value is normalized by dividing it by the reference density from the previous evaluation.

Table 3: Fluid properties used in the karstic settings

Temperature [°C]	**Pressure** [MPa]	**Reference Density** $[\frac{\text{kg}}{\text{m}^3}]$	**Viscosity** $[\frac{\text{kg}}{\text{m s}}]$	**Diffusion Coefficient** CO_2 $[\frac{\text{m}^2}{\text{s}}]$	γ
8	0.1	999.85	1.39×10^{-03}	1.18×10^{-09}	0.4
20	0.1	998.20	1.00×10^{-03}	1.60×10^{-09}	0.4

Table 4: Geological scenarios for CCS

Scenario	**Temperature** [°C]	**Pressure** [mPa]	**Salinity** $[\frac{\text{mol}}{\text{kg}}]$
S	55	15.5	1
C	37.5	15.5	1
D	115	35.5	1

Table 5: Fluid properties used in the CCS-Systems

Scenario	**Reference Density** $[\frac{\text{kg}}{\text{m}^3}]$	**Viscosity** $[\frac{\text{kg}}{\text{m s}}]$	**Diffusion-Coefficient** CO_2 $[\frac{\text{m}^2}{\text{s}}]$	γ
S	1025.96	0.56×10^{-03}	3.53×10^{-09}	0.47
C	1037.39	0.76×10^{-03}	2.47×10^{-09}	0.42
D	996.46	0.28×10^{-03}	7.14×10^{-09}	0.43

3.6 Validation of the OpenFOAM Model and Lessons Learned from It

Before using the OpenFOAM numerical simulator for generating the data for this study, the specifically modified model, including the model assumptions, the discretization scheme, the setting and choice of fluid properties, was validated. For that purpose, the experimental data from Class et al. (2020) were used. In that study, a fracture of 1 cm aperture was subjected to varying partial pressures, pCO_2, at 8 °C . For the simulation runs, the Courant criterion (CFL number) was kept below 1. The grid is a simple regular quadratic grid with 1 mm discretization length. The front velocities measured in the experiment and determined by the OpenFOAM runs were compared with the results provided by Table 6. Given the uncertainties that are also associated with the experimental data (Class et al., 2020), the agreement between simulation and experiment is very reasonable.

Experiences from performing the validation runs led to specifications and accuracy criteria for the simulation of the above-explained karst and CCS scenarios. A minimum of 10 cells is needed in the direction of the aperture, while the length of the cell should not exceed 1 mm. The Courant number was kept below 1. For very small apertures, holding on to regular quadratic grid while having 10 cells in a cross-section, would dramatically increase the computational costs. For that reason we chose to allow for aspect ratios of up to 3 in the case of the smallest aperature of 1 mm.

For detailed numerical settings, see Appendix B.

4 Results and Discussion

4.1 Dimensionless Fluxes Obtained from Numerical Scenario Simulations

For a first evaluation and interpretation of the results of the numerical scenario simulations, the classical approach from the CCS-related porous-media literature on convective dissolution is used, where fluxes are non-dimensionalized to retrieve a flux effi-

Table 6: Comparison of finger-front velocities from validation simulations to experimental data.

Case	**Concentration** $[\frac{mol}{mol}]$	**Method**	**Finger-Front Velocity** $[\frac{cm}{min}]$
V_I	1×10^{-3}	Experiment	1.33
		Simulation	1.69
V_{II}	5×10^{-4}	Experiment	0.84
		Simulation	1.13

ciency $\langle F \rangle$ (for interpretation see Equation (1)), using a unique and constant value for the characteristic velocity (detailed procedure is described in Appendix C). This approach allows for a simplified analysis of the results by scaling fluxes with a finger-front velocity that was evaluated for all fractures at the same reference control height, here h_{30}. The analysis is subdivided below into three categories, each corresponding to a distinct temperature regime: 8 °C, 20 °C, and typical reservoir conditions for CCS. For each category, the curves of the flux efficiency over dimensionless time τ ($\tau = t\frac{v_c}{d}$ with v_c being the finger-front velocity evaluated at control height h_{30}) are analyzed. The details of the non-dimensionalization procedure for the calculated fluxes can be found in Appendix C2.

4.1.1 Karstic-System

Two of the temperature categories are related to the karstic systems. Without specific evidence, we label the temperature of 20°C as related to more tropical karst systems, while we have good data to associate the 8°C regime with karstic systems of the Swabian Jura in southern Germany (Class et al., 2023).

The semi-logarithmic plot for 20°C in Figure 3 shows a distinct clustering related to the different apertures. The flux efficiency for the fractures with an aperture of 1×10^{-01} m is consistently lower with $\langle F \rangle < 1 \times 10^{-2}$. In contrast, the fractures with 1×10^{-02} m aperture end up far above that value with $\langle F \rangle > 2 \times 10^{-02}$. Furthermore, a more rapid stabilization of the flux efficiency, $\langle F \rangle$, can be observed for the small aperture of 1×10^{-02} m, which is distinctly different for the large apertures. The period, when quasi-equilibrium is then established, is still featuring minor oscillations for the large apertures. Even more pronounced are the observed oscillations for the small aperture during the equilibrium period. The double-logarithmic plot in the figure's inset zooms into the transient flux behavior in the initial phase, where small, sharp spikes suggest the observed occurrence of first instabilities. This indicates that the onset in dimensionless time (τ_o) is $\approx 1 \times 10^{-02}$ for the small apertures and $\approx 1 \times 10^{-01}$ for the larger apertures.

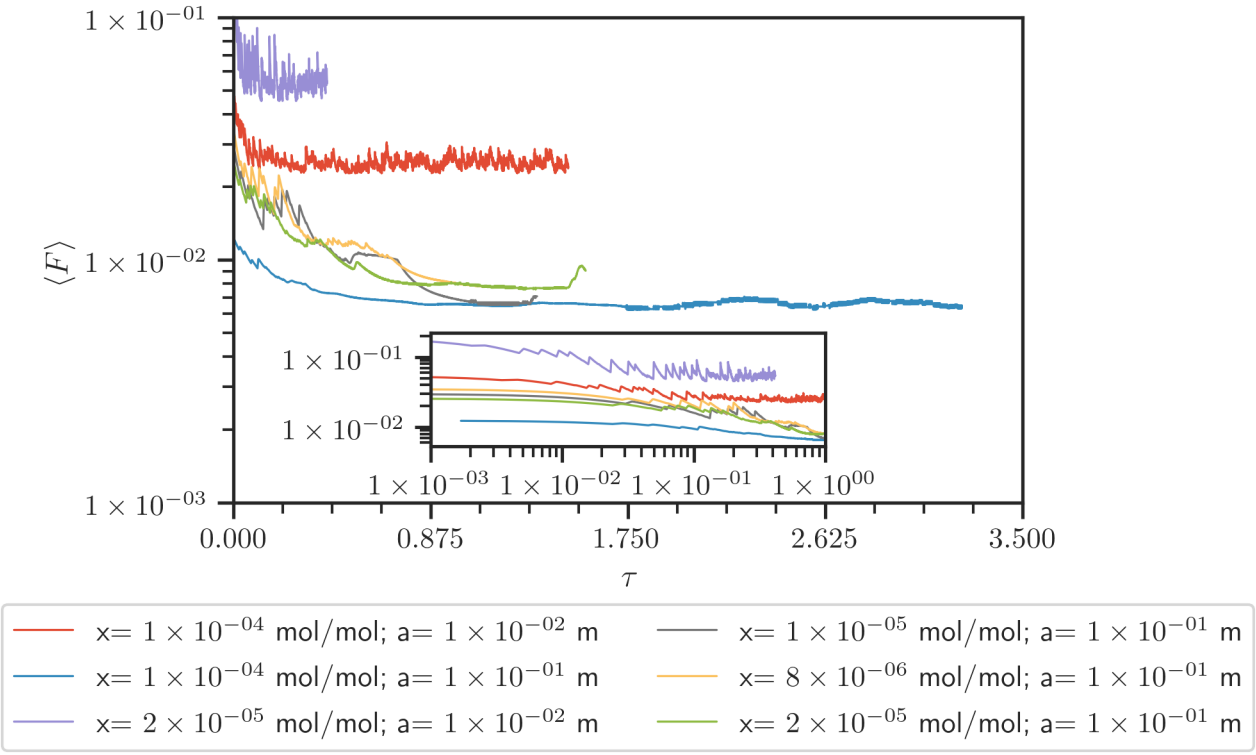

Figure 3: Semi-logarithmic plot of characteristic flux $\langle F \rangle$ as a function of dimensionless time τ for a series of applied CO_2 concentrations x and apertures a in karst settings at a constant temperature of 20 °C . The inset is a double-logarithmic plot offering a detailed view of the initial phase illustrating the changes in flux at the onset of the process. It can be observed that all curves tend to reach a constant $\langle F \rangle$, while this occurs not at the same dimensionless time and at the same magnitude.

For a temperature of 8°C , the semi-logarithmic plot in Figure 4 shows again a pronounced clustering according to the fracture apertures, similar to the observations at 20°C . The flux efficiency for fractures with an aperture of 0.01 m stabilizes more swiftly, achieving a higher final value with $\langle F \rangle$ between $\approx 5 \times 10^{-02}$ and $\approx 3 \times 10^{-02}$. In contrast, for the larger apertures, $\langle F \rangle$ ranges from approximately 1×10^{-02} to 6×10^{-03}. During the equilibrium period, larger apertures exhibit minor oscillations. On the other hand, the smaller 0.01 m aperture shows significantly larger oscillations, suggesting that adjustments are less easily occurring due to the smaller aperture size and larger viscous resistance. Similar to the findings for 20 °C , small, sharp peaks suggest the observed occurrence of first instabilities. The onset in dimensionless time (τ_o) is as before $\approx 1\times 10^{-02}$ for the small apertures and 1×10^{-01} for the larger openings. Note that this does not mean that the physical (dimensional) onset occurs earlier for smaller fractures.

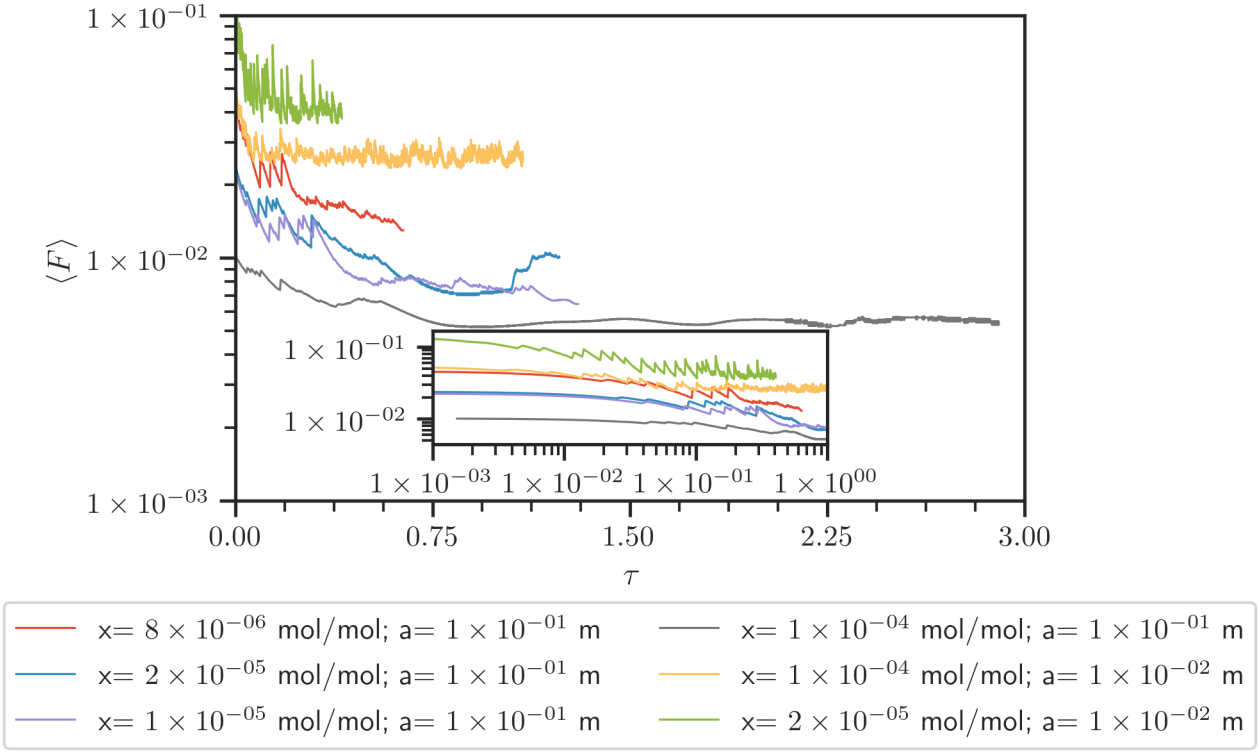

Figure 4: Semi-logarithmic plot of characteristic flux $\langle F \rangle$ as a function of dimensionless time τ for a series of applied CO_2 concentrations x and apertures a in karst settings at a constant temperature of 8 °C . The inset is a double-logarithmic plot offering a detailed view of the initial phase illustrating the changes in flux at the onset of the process. Observations are in analogy to Fig. 3.

4.1.2 CCS-System

The semi-logarithmic plot in Figure 5 illustrates the flux efficiency, $\langle F \rangle$, for the three simulated scenarios, labeled with S, C, and D. A discernible difference in the stabilization of $\langle F \rangle$ is observed among the scenarios. In Scenario S, the flux stabilizes at a higher value of approximately 4×10^{-2}, whereas Scenarios C and D converge to a slightly lower value near 3×10^{-2}. The equilibrium period for Scenario S is characterized by pronounced oscillations, reflective of significant flux fluctuations. In contrast, Scenarios C and D exhibit more subdued oscillations. The inset's double-logarithmic scale provides a detailed view of the initial transient behaviors, with the marked fluctuations in Scenario S potentially indicating the early onset of instabilities. This variation in the initial flux behavior suggests that the scenarios may differ in their respective timings for the development of instability and subsequent flux adjustments.

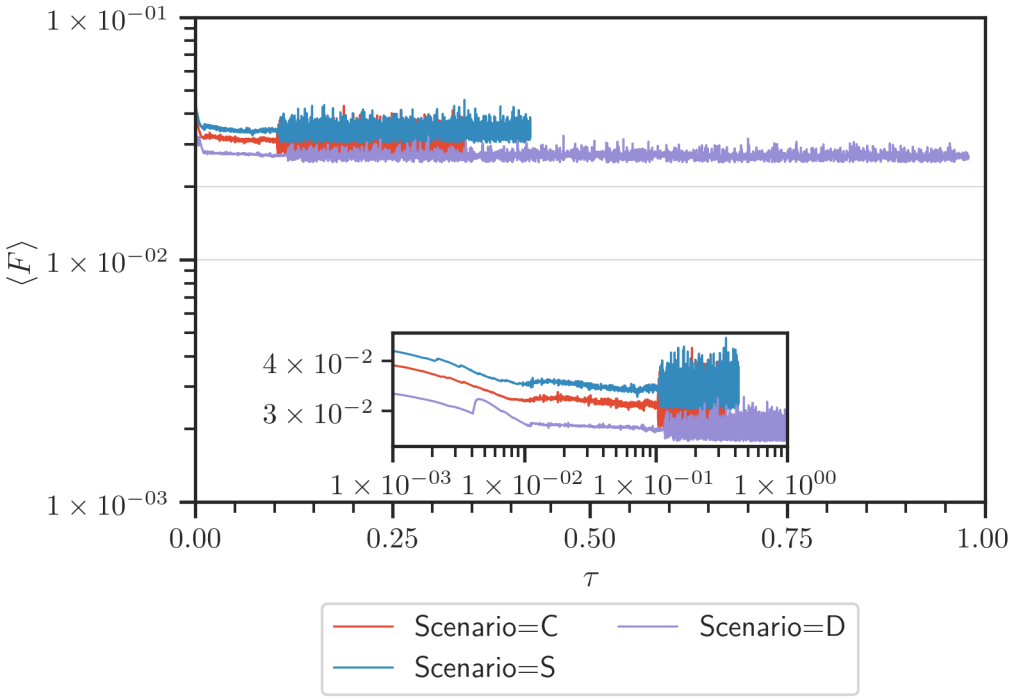

Figure 5: Semi-logarithmic plot of characteristic flux $\langle F \rangle$ as a function of dimensionless time τ for various CCS scenarios labeled S, D, and C, which represent different ambient conditions or temperature settings. The inset is a double-logarithmic plot highlighting the early-time flux behavior in detail, illustrating the distinct response for each scenario. A constant flux is observed for all cases at very early dimensionless time, while fluctuations increase distinctly after $\tau = 1 \times 10^{-02}$ and 1×10^{-01}

4.1.3 Preliminary Summarized Interpretation of Simulation Results

The results of the numerical scenario simulations described in Table 1 and Table 2 highlights the complex interplay between concentration, aperture, and temperature and their influence on flux efficiency, $\langle F \rangle$, over τ. Simulations with a 1 mm aperture did not exhibit fingering under karstic conditions, which is evidence that a threshold aperture exists for this phenomenon to occur. The rest of the simulations with fingering are shown in Figures 3 to 5 and show an initial diffusion-dominated regime with a rapid influx followed by a steady decrease due to the thickening of the diffusion layer at the gas-water interface and a corresponding decrease in the concentration gradient.

As the simulations progress, the onset of fingering or natural convection is observed at varying times across the different scenarios. Spikes in the flux are indicative of the commencement of fingering. Notably, the steady-state values observed do not align with the flux-efficiency values reported in the literature of $\langle F \rangle \approx 1 \times 10^{-01}$ to 1×10^{-02} (De Paoli et al., 2020), $\langle F \rangle \approx 1.7 \times 10^{-02}$ (Hesse, 2008; Green & Ennis-King, 2018), or $\langle F \rangle \approx 2 \times 10^{-02}$ (Elenius & Johannsen, 2012). Simulations with apertures of 1 cm and smaller tend to a slightly higher flux efficiency, while simulations with 10 cm aperture tend to a lower flux efficiency. It is, however, not surprising that the literature values cannot be reproduced more accurately, since the chosen characteristic velocity used for scaling is defined differently. In porous-media research, a Darcy-velocity is calculated, while we evaluate a finger-front velocity from a Navier-Stokes model at a given control height. We remark further that the choice of a unique control height implies that the

real finger-front velocities are in general not equal to this calculated velocity. Furthermore, a Darcy-velocity is a continuity-based average velocity, while a finger-front velocity is not averaged. In comparison to De Paoli et al. (2020), where the 1 mm aperture shows already a distinctly different flux efficiency, here the main difference is encountered between 1 and 10 cm aperture. This could have several reasons; one is that the use of a Darcy-velocity in De Paoli et al. (2020) can lead to that effect; second, there might be another jump in efficiency in aperture sizes not studied in this study. Irrespective of the difficulty in comparing the results here with the literature, the main conclusions remain: smaller fractures do have higher fluctuations during the fingering regime, and fractures with an aperture of 10 cm show a completely different flux efficiency. Furthermore, the amount of oscillation seems to follow a pattern: the greater the driving force, i.e. the concentration and hence the density difference, the smaller the oscillations; the greater the viscous forces resisting the detachment of the fingers, the larger the oscillations. The interpretation is that the easier it is for a finger to detach, given the driving force and the resisting force, the smaller the oscillations will be due to a more continuous process.

4.1.4 Notes on the Comparison of Onset Times

Finding the onset time proved to be a challenge. In comparison to CCS-related studies, we could not find an equally distinct minimum in the CO_2 flux that would indicate the transition from the diffusive to the convective regime. Visual inspection showed that apertures smaller than 1 cm have their first distinct spike at around $\tau \approx 1 \times 10^{-02}$, while apertures of 10 cm have their first spike in the order of $\tau \approx 1{\times}10^{-02}$ to $1{\times}10^{-01}$. For instance, Hesse (2008) found a relationship in the context of CCS using porous-media flow equations.

$$\tau_o = 6215 \frac{\phi \mu^{11/5} D^{6/5}}{(k \Delta \rho g)^{11/5} H^{1/5}} = 6215 \frac{\phi \mu^{11/5} D^{6/5}}{\left(\frac{a^2}{12} \Delta \rho g\right)^{11/5} H^{1/5}} \tag{21}$$

One could now compare both the estimated onset times from our study to non-dimensional onset time τ_o from the literature. Such a comparison is, however, not very useful since the definition of u_c to scale the non-dimensional time is different. Still, the physical/dimensional onset times in seconds can be compared to other studies. The order of onset time found in this study is 10 s. In comparison, Elenius and Johannsen (2012) found onset times between 40 days and 700 years. Ennis-King (2005) reported values as low as 0.0026 years, i.e., $\approx$ 1 day. In conclusion, for predicting effective entry rates into a fracture we recommend to neglect the onset time. For a fractured CCS reservoir, the mass of CO_2 transported by convective mixing within fractures is probably not significant. Nonetheless, it might be worth to scrutinize whether a quick perturbation caused by induced instabilities in fractures could lead to an earlier larger scale convective mixing in a CO_2 storage reservoir.

4.2 Flux, Flux Efficiency and 3-Dimensional Effects

Having identified the aperture as the dominant factor influencing the temporal evolution and the final quasi-stationary value of the flux efficiency, $\langle F \rangle$, two exemplary showcases, differing only in aperture, are compared in the following with respect to the evolution of the fingers.

Figure 6 consists of multiple plots arranged to illustrate the flux behavior through two fractures of 10 cm and 1 cm aperture under otherwise identical specific conditions. In the top row, two temporal developments of flux are presented: the left one depicts a fracture of 10 cm aperture at a temperature of 8°C , having a x_{CO_2} of $1{\times}10^{-04}$ mol/-mol at the boundary, while the right one represents the same setting but with a smaller aperture of 1 cm. The analysis of the 10 cm fracture reveals distinct periods in the flux behavior. Initially, signs of instability become apparent after around 200 s, followed by a decrease of the flux until 600 s. A significant peak is observed between 600 and 1200 s,

after which the flux then stabilizes, albeit with a slight tendency towards minor fluctuations after 3600 s. In contrast, the 1 cm fracture maintains a quasi-steady flux value already from 200 s onwards, however with a more pronounced noise.

Contour plots corresponding to the 10 cm fracture visually correlate these observations with comprehensive mechanisms. Early stages are characterized by numerous small instabilities that gradually merge into multiple, larger fingers until 600 s, beyond which then a single dominant finger emerges, indicating the attainment of a quasi-stationary flux. Conversely, the contour plots for the 1 cm fracture reveal a persistent parabolic profile throughout, with no evidence of convergence towards a singular finger forming.

Merging of fingers is not only discovered in our 3-D simulations. Also Elenius and Johannsen (2012) found merging fingers and even reported that 'During the time that fingers merge, the vertical movement seems to be restricted in favor of the horizontal movement' ((Elenius & Johannsen, 2012), Figure 7). This is in agreement with the findings elaborated in this sectionr, i.e., the number of fingers completely changes the dynamics of the system.

In analyzing the flux efficiency, $\langle F \rangle$, it becomes evident that fractures maintaining a parabolic profile exhibit significantly higher flux efficiency compared to those showing 3-D effects. Remarkably, the smaller apertures even surpassed the larger apertures when it comes to actual flux of CO_2 per area and time. This shows that the difference in flux efficiency is so significant that a smaller resistance against flow, i.e., larger aperture, cannot balance this phenomenon. Furthermore, fractures with 3-D features pose considerable challenges for predictions due to the complexity introduced by the merging of fingers. This formation process consists of several stages, each of which must be captured in any predictive model to reflect the evolving dynamics of the flow; alternatively the merging could be ignored and only the final $\langle F \rangle$ considered, while keeping in mind that this will cause an inaccuracy in the prediction for the early stages of fingering. The results of this study could not reveal details about the transitioning from smaller fractures with a parabolic profile to larger fractures with 3-D effects, whether this occurs continuously or rather as jumps in terms of the flux efficiency. More numerical experiments are required, which is beyond the scope of this study.

4.3 Rayleigh-Number Invariance of Flux Efficiency

In Section 2.3, it was shown that the adopted definition of the Rayleigh number can be interpreted as being of the Péclet-number type. As elaborated before, the literature provides evidence that $\langle F \rangle$ is Rayleigh invariant in CCS reservoirs. Recalling once again their definitions,

$$\langle F \rangle = \frac{F}{u_c \rho x_{\mathrm{CO}_2,c}}$$

and

$$Ra = \frac{u_c L_c}{D},$$

it follows that F is a linear function of u_c and independent of D and L_c in porous-media CCS reservoirs; in other words, the larger u_c, the larger is the advective flux. Previous results (Sections 4.1 and 4.2), however, revealed a more nuanced picture. While each fracture at some point reaches a constant flux efficiency, their respective values differ from case to case. The diffusion coefficient D is a given material property. Note that depth d, which is commonly used for L_c in porous-media research was held constant there. Let us now question this assumption and try to identify an appropriate definition of the characteristic length.

We observed previously that depending on 3-D effects, a constant flux efficiency establishes only after the merging of fingers is complete, i.e., after a certain distance from the gas-water interface (parameter χ in Figure 1). We hypothesize now that the char-

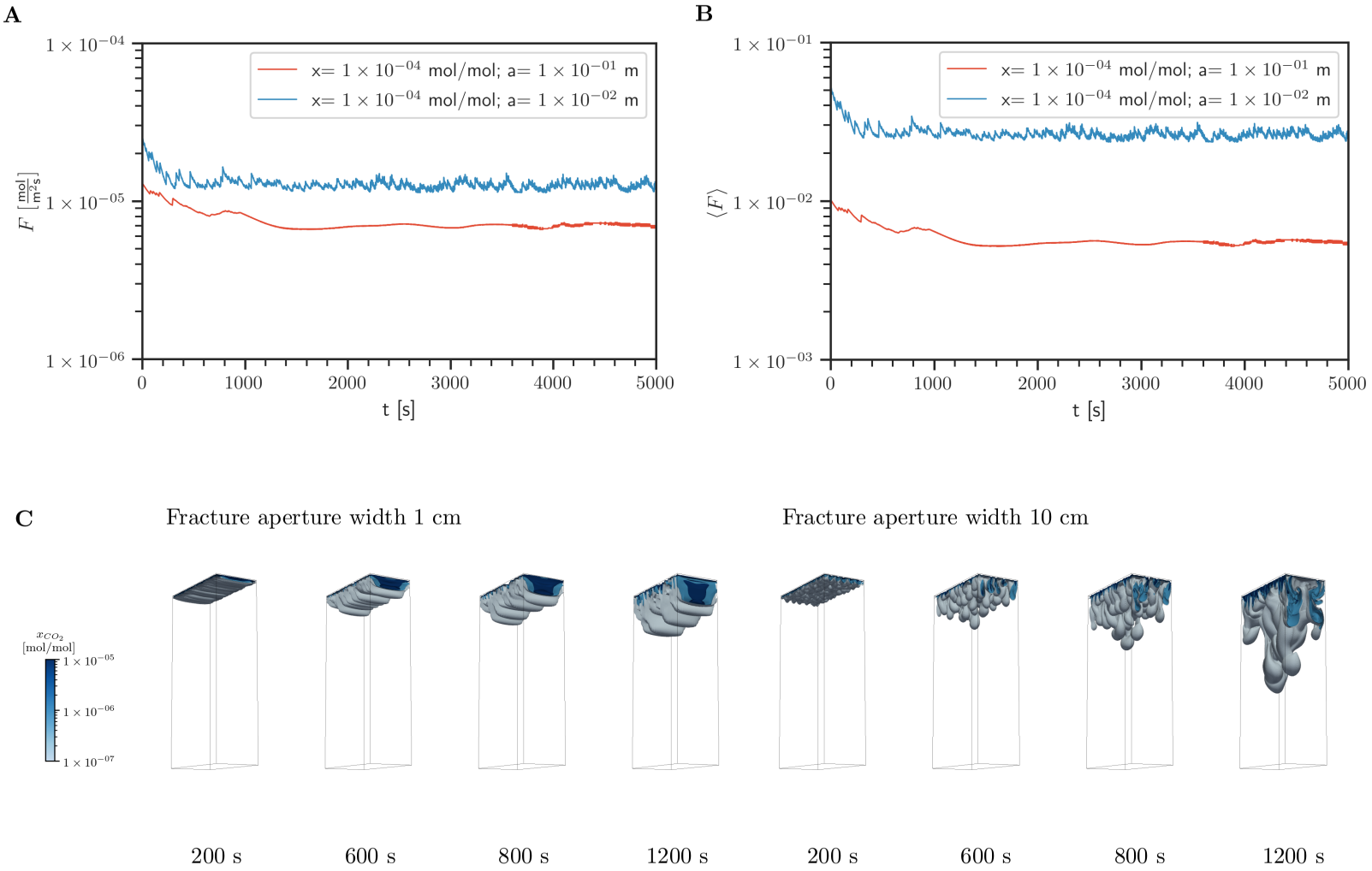

Figure 6: Comparison of two distinct apertures (1 cm and 10 cm), both subjected to a CO_2 concentration of 1×10^{-04} mol/mol at the top boundary at a temperature of 8 °C . **A:** Plot of physical flux [mol/(m^2 s)] versus physical time [s], showing flux adjustments after the start of fingering for the larger aperture (red) while the smaller aperture remains constant. **B:** Plot of flux efficiency against physical time [s]. Note the corresponding change in flux efficiency after the onset of fingering for the larger aperture (red), while the small aperture remains constant. **C:** Contour plot displaying the evolution of the finger front for the 1 cm aperture (width is scaled by a factor of 10 for visualization) and the 10 cm aperture. A correlation between the appearance of the fingers and the flux, flux efficiency, can be observed.

acteristic length is the length where the flux efficiency is fully developed. It is further remarked that the reason for the different characteristic lengths is the development of a boundary layer (for theory see Section 2.4). Using the Schmidt number,

$$Sc = \frac{D}{\nu}\,,$$

allows converting the critical Rayleigh number into a Reynolds number

$$Re = \frac{u_c L_c}{\nu}\,.$$

Using Equation (20) we find that the derivative of the boundary layer with respect to χ is as follows:

$$\frac{\partial a^\star}{\partial \chi} = \begin{cases} 0, & \text{for } a \leq 2\delta \\ \frac{-5}{Re_\chi{}^{1/2}}, & \text{for } a > 2\delta \end{cases} \tag{22}$$

The conclusion is that the critical Rayleigh number corresponds to a certain depth at which a posed condition (defined by Ra and Sc) on the change in boundary layer thickness is satisfied. The validity of this idea is analysed below.

For each simulation run, the flux efficiency was determined during various time periods using the median flux and the breakthrough velocity between control heights. The results can be seen in Figure 7. Note that this new scaling approach introduces now a non-continuous course of the $\langle F \rangle$ curves due to the non-constant and non-continuous choice of the front-velocity as it is evaluated segment-wise between two control heights, see exemplary curves in Figures D1 and D2 and compare with the respective continuous curves in Figures 3 to 5 where a constant front-velocity was used. The non-continuity of front-velocity and $\langle F \rangle$ with respect to τ is not addressed in the further, while it is also not of importance for our evaluation.

Figure 7 presents an analysis of flux efficiency as a function of an evaluated Rayleigh number, where for each calculated data point the characteristic length is defined as the respective depth at which both flux and velocity are evaluated. Based on our observation, we justify to assume for a curve fitting that flux efficiency, $\langle F \rangle$, initially starts with a high value, dominated by diffusion mechanisms at the gas-water interface. $\langle F \rangle$ declines subsequently and approaches an asymptotic value. We can then introduce the following approach to fit the calculated data points with continuous curves:

$$\langle F \rangle (Ra) = \frac{1}{\lambda_{\langle F \rangle} Ra} + \langle F \rangle_\infty \tag{23}$$

The relationship between the fitting parameters is illustrated in Figure 8. $\langle F \rangle_\infty$ is the asymptotic (final) efficiency for a (hypothetically) infinitely deep fracture, while $\lambda_{\langle F \rangle}$ is a measure of how fast the efficiency declines. We introduced a criterion to indicate when $\langle F \rangle$ approaches its quasi-constant final value. For that we assumed that 1.2 times the final efficiency value $\langle F \rangle_\infty$ is an appropriate measure to demarcate flux stabilization. The value of 1.2 was chosen based on expert judgement without any derivation. The detailed derivation for the black line in Figure 7, denoting $\langle F \rangle_{crit} = f(Ra_{crit})$, is given in Appendix Appendix E. Notably, the analysis highlights that the fits for fractures measuring 10 cm in aperture exhibit a significantly higher critical Rayleigh number alongside a reduced efficiency. This underscores the impact of fracture apertures on the dynamics of convective fluid flow and its efficiency to transport CO_2, with larger fractures demonstrating a distinct behavior characterized by lower efficiency and altered critical thresholds for flux stabilization.

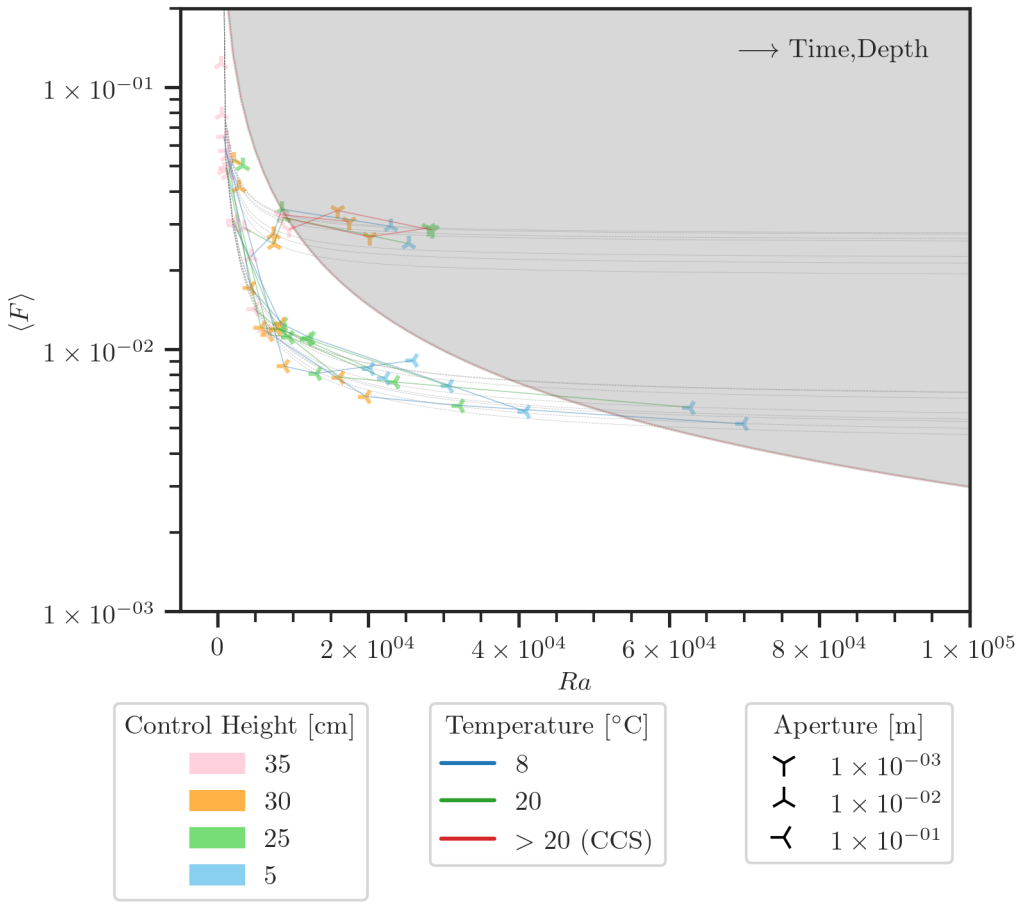

Figure 7: The graph depicts the relationship between the flux efficiency $\langle F \rangle$ and the Rayleigh number, Ra, for different control heights and temperature conditions. The data points are colored based on control heights: 5 cm (blue), 25 cm (green), 30 cm (orange), and 35 cm (red), with further distinction for temperatures at 8°C (blue lines), 20°C (green lines) and CCS-reservoir conditions (red lines). The shade to the right of the line of critical Ra values indicates the region of Rayleigh-invariance for the fitted curves.

The parameter combinations found in the fitting of Equation (23) are shown in Figure 8. The correlation is obvious and underlines that the initial drop of the efficiency, attributed to $\lambda_{\langle F \rangle}$, correlates strongly with the final efficiency, $\langle F \rangle_\infty$.

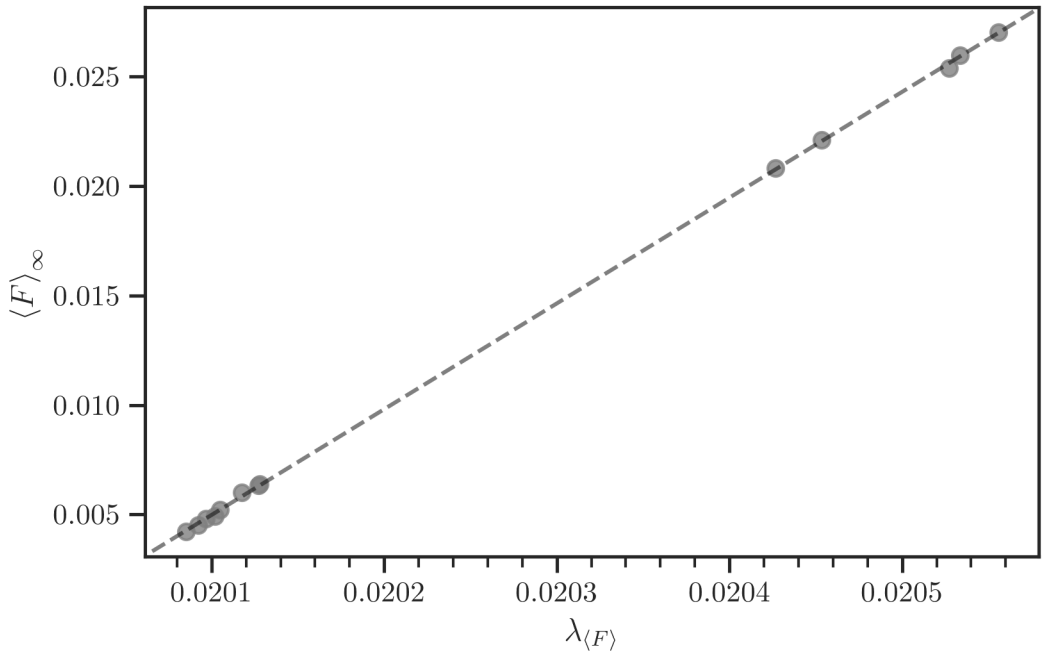

Figure 8: The scatter plot illustrates the results of a curve-fitting approach, using Equation (23). Each data point corresponds to a set of fitted parameters $(\lambda_{\langle F \rangle}, \langle F \rangle_\infty)$. The relationship between the two was found to fit with $\langle F \rangle_\infty = 48.299\lambda_{\langle F \rangle} - 0.9658$. The lower left dots are the results for the large apertures, while the upper right have smaller apertures.

4.4 Predictions for Efficiency and Fluxes

We have formulated as aim of this study that the evaluation and interpretation of the performed numerical experiments with highly resolved OpenFOAM simulations should enable us finally to estimate CO_2 influx rates due to convective dissolution, admittedly for the beginning only in academically idealized fractures. For this purpose, we propose a procedure as explained in the following.

We have found previously that there is a critical Rayleigh number above which the flux efficiency approaches a constant value or, in other words, above which the flux efficiency is Rayleigh-invariant. Recalling Equation (1), it is proposed that this equation holds as soon as the conditions in a fracture of interest surpass the critical Rayleigh number. We can assume that the boundary-layer developments are the primary reason for the observed differences in the curves of the flux efficiency plotted over the Rayleigh number. In accordance with our definition of the Rayleigh number, we can make use of the Schmidt number to derive a critical Reynolds number which is associated to a condition of the derivative of the Prandtl-Blasius boundary-layer development (Equation (22)). To actually predict the flux rates, it is first of all required to know $\langle F \rangle$ and u_c, as well as the vertical distance from the gas-water interface below which these estimates hold.

Given that, it is then proposed to first find an estimate for the final efficiency, $\langle F \rangle_\infty$, which can be transferred into a critical Rayleigh number. Using the boundary-layer theory and the beforehand determined critical Rayleigh number allows then to find a u_c and a L_c, with L_c representing the distance, χ, that the fingers need to reach from the gas-water interface.

In Appendix E1, the details of how to determine the characteristic velocity and the characteristic distance to the gas-water interface from a critical Rayleigh-number are provided. Applying this approach leads to results for the estimated velocity compared to the observed velocity as shown in Figure 9. The dots are highlighting velocities found in the data that also satisfy the condition of $Ra > Ra_{crit}$; they obviously show very good agreement between the proposed procedure and the data.

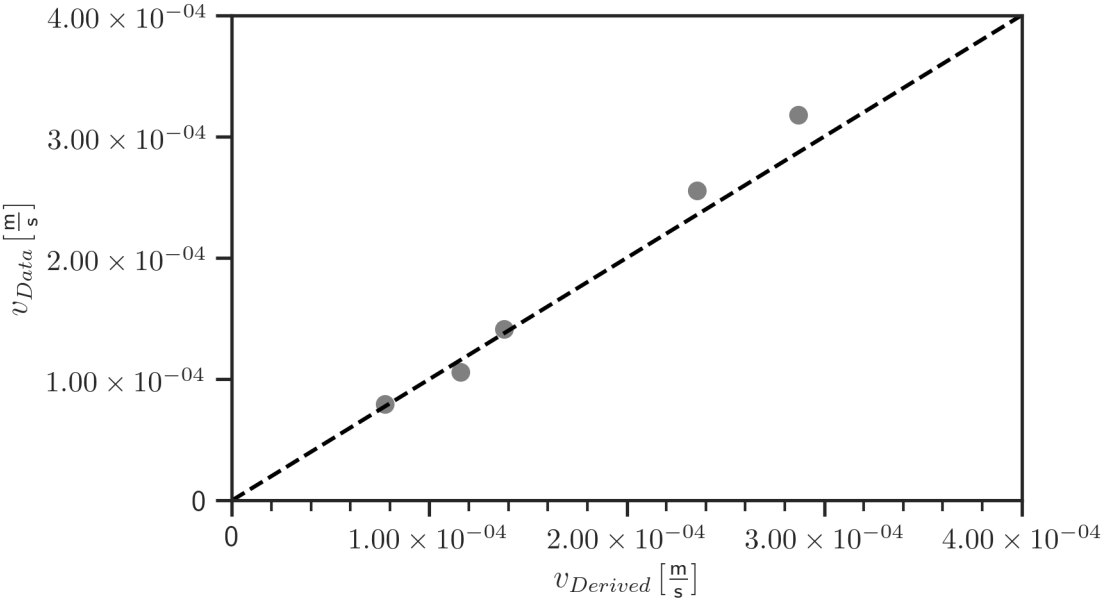

Figure 9: This figure illustrates the comparison between measured velocity from numerical experimental data and velocity derived from data for given final efficiencies $\langle F \rangle_\infty$. The velocity is derived from the relationship between the final flux efficiency, the critical Rayleigh number, the Schmidt number, the Reynolds number and a boundary layer development condition (for details see Appendix E1). As can be seen, it is possible to derive a characteristic velocity from a critical Rayleigh number, without the need to predict the characteristic velocity.

Finally, to allow for a prediction of flux rates, it is required to robustly estimate the critical flux efficiency or the fitting parameter $\langle F \rangle_\infty$. From that, the critical Rayleigh number can be determined as well as subsequently the other required values, see above. We suggest to use first of all three dimensionless numbers, denoted below as Π-quantities (inspired by Buckingham's Π-Theorem), to reduce the number of involved parameters.

- $\Pi_1 = \frac{\Delta\rho}{\rho_0}$
- $\Pi_2 = \frac{\nu}{D} = Sc$
- $\Pi_3 = \frac{a^3 g}{\nu^2}$

The suggested procedure yields finally the following relationship:

$$\langle F \rangle_\infty = \frac{0.268}{\Pi_1^{1/6} \Pi_2^{1/6} \Pi_3^{1/5}} \tag{24}$$

A comparison of the values determined in this way with the calculated data of the numerical experiments is given in Figure 10.

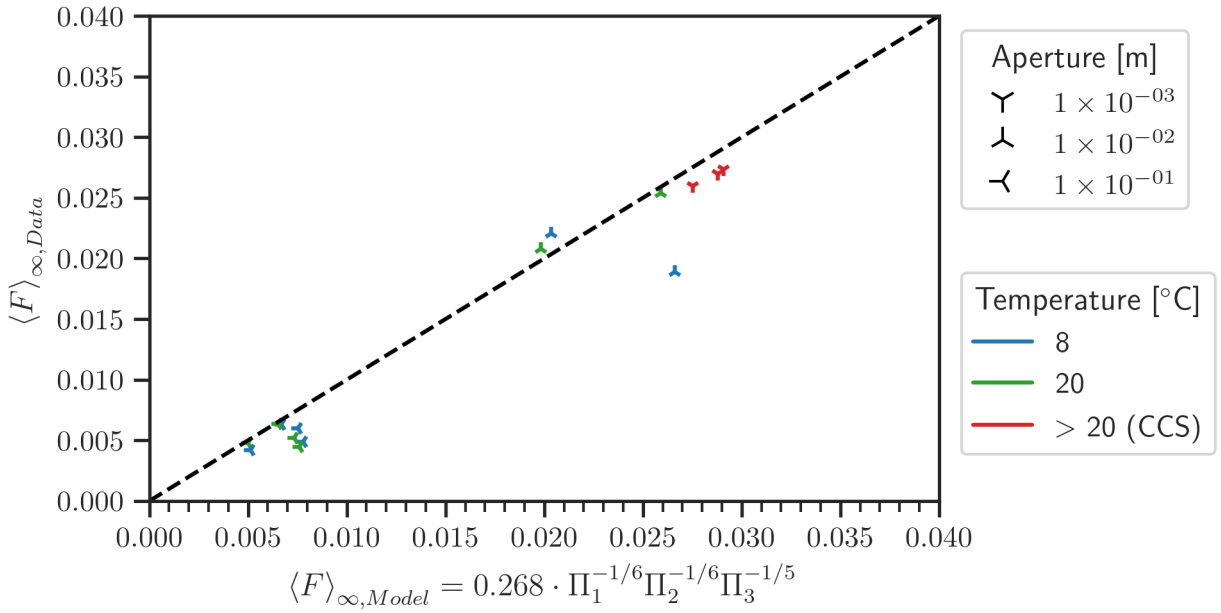

Figure 10: Predicted final flux efficiency, $\langle F \rangle_\infty$, against the $\langle F \rangle_\infty$ from the numerical experiments. The data points are are colored based on the case temperature; 8 °C (blue), 20 °C (green) and the CSS related simulations are in red. Additionally the fracture aperture is shown with different markers. The gap in flux efficiency $\langle F \rangle$ between the 10 cm and and 1 cm apertures is prominently visible, also referred to as different modes, while it seems there is no gap or transition of modes between 1 mm and 1 cm. In general the model displays the trend accurately, however due to the lack of data between 1 and 10 cm continuity between the modes remains unclear for now.

4.4.1 Algorithm for Flux-Predictions

The input values are: $\rho_0, \Delta\rho, a, \nu, D, g$ and x_{CO_2}

- Calculate $\langle F \rangle_\infty = \frac{0.268}{\Pi_1^{1/6}\Pi_2^{1/6}\Pi_3^{1/5}}$
- Use $Ra_{crit} = \frac{48.299}{0.2\langle F \rangle_\infty(\langle F \rangle_\infty - 0.9685)}$
- Calculate $\langle F \rangle$ from Equation (E7)
- Solve the system of equations described in Equation (E10) for u_c
- Use Equation (1) to predict the CO_2-flux per aperture-area.

4.4.2 Test of Predictions

The simulations employed to validate the model (see Section 3.6) were explicitly excluded from the above explained fitting process. This deliberate separation allows for an evaluation of the model's predictive capabilities using a set of data akin to a test dataset, distinct from the training dataset. The outcome of this evaluation is detailed in Tables 7 and 8.

Table 7: Comparison of $\langle F \rangle_\infty$ and u predictions with data

	$\langle F \rangle_\infty$			u		
Case	$\langle F \rangle_{\infty\text{pred}}$	$\langle F \rangle_{\infty\text{data}}$	Error	u_{pred}	u_{data}	Error
V_I	1.39×10^{-02}	7.20×10^{-03}	9.23×10^{-01}	1.13×10^{-04}	2.82×10^{-04}	-5.99×10^{-01}
V_{II}	1.55×10^{-02}	1.04×10^{-02}	4.96×10^{-01}	9.34×10^{-05}	1.88×10^{-04}	-5.02×10^{-01}

Recalling Equation (1) allows for directly using the errors from $\langle F \rangle$ and u_c, calculating an error for the overall physical flux F:

Table 8: Comparison of F predictions with data

	F	
Case	F_{pred}	Error
V_I	8.57×10^{-05}	-2.29×10^{-01}
V_{II}	4.03×10^{-05}	-2.55×10^{-01}

4.4.3 CO_2 Flux Estimates under Karstic Conditions

Class et al. (2021) investigated how much CO_2 could enter a water body per unit time. The predictive approach developed in this study was used to predict entry rates under the same conditions. In Table 9 it can be seen that this study is consistent with their estimated fluxes of $\approx$ 10 g/m^2 month.

Table 9: Predicted CO_2-fluxes in [g/m^2 month] into a fracture subjected to 16000 ppm p_{CO_2} at 8 °C .

Aperture Size [m]	CO_2-flux $[\frac{g}{m^2\ month}]$
0.01	33.16
0.02	24.92
0.03	17.27
0.04	16.48
0.05	14.67
0.06	15.83
0.07	12.99
0.08	12.49
0.09	13.46
0.10	13.00

It is noted, that the flux per unit area and time increases with decreasing aperture, while this behavior is obviously non-linear. Furthermore, this table needs to be taken with care for very small apertures, since the fingering phenomenon will not occur when viscous resistance is too high relative to the driving force, i.e., the density difference.

5 Conclusions

Period of constant flux and flux efficiency in convective dissolution in fractures Similar to the observation made for porous media, the flux F and flux efficiency $\langle F \rangle$ due to CO_2 convective dissolution in open fractures reaches a constant value after some time. In contrast to porous media, the fractures revealed also a period of fingering during which flux and flux efficiency are still changing. The onset of fingering does not directly lead directly to a period of constant flux.

Flux efficiency values exhibit modes The flux behaviour, and hence $\langle F \rangle$, within the fractures shows a distinct difference between fractures in which 3-D fingering effects occur and those exhibiting a parabolic profile. The resulting flux efficiencies $\langle F \rangle$ are so different that fractures with smaller apertures have a higher flux of CO_2 within the fracture than their larger counterparts. The exact nature of the transition between modes of flux efficiency, whether it is a smooth transition or a distinct jump, remains unresolved for now.

How to predict CO_2 entry rates in a water-filled fracture We propose that it is crucial to identify a Rayleigh invariance, analogous to what has been observed in studies of porous media. The analysis established a clear relationship between the period of stable flux efficiency and a case-dependent critical Rayleigh number. It was observed that exceeding this critical Rayleigh number correlates with fingers extending beyond a certain distance to the gas-water interface. This distance is significantly influenced by the fracture aperture and, thus, varies with the developing boundary layer. Based on the interaction of critical Rayleigh number and boundary layer development, a novel prediction approach has been developed and experimentally validated. The technique employed here provides a reliable, physically based framework, within the limitations of the data, for scaling up CO_2 flux predictions due to convective dissolution from open fractures to larger field-scale models. This strategy provides a viable way of incorporating precise local-scale phenomena into larger-scale geospatial models and the possibility to extend this work with appropiate boundary layer assumptions.

Implications for karst research The estimates of potential CO_2 fluxes into fractures derived from this study closely match those from previous research, such as Class et al. (2021), confirming that under certain conditions the amount of CO_2 dissolving into a fracture could be as high as several tens of grams per square meter per month. Specifically, this study has added insights about how the fluxes per unit area increase with decreasing fracture aperture. Thus, many small fractures lead to a higher convective CO_2 flux than fewer but larger fractures. This highlights the relevance of convective CO_2 dissolution in karstic systems to be considered for speleology.

Current limitations, open questions, and prospects The prediction of the final flux efficiency is currently limited by open questions regarding the understanding of the transition between three modes, i.e., (i) no fingering, (ii) fingering exhibiting a parabolic profile, and (iii) fingering exhibiting 3-D effects. The first open question is concerned with the conditions under which fingering starts, i.e., at which aperture size for a given concentration? The second question has to addresses whether the shift from parabolic to 3D flow behavior is a jump-like phenomenon.

A separate, yet significant, unresolved issue concerns the onset times in open fractures, which are typically small and, thus, considered negligible for predicting long-term effective fluxes resulting from the convective dissolution of CO_2 in these structures. In the realm of carbon capture and storage (CCS), the rapid initiation of convective mixing within small fractures and fissures may influence larger-scale dynamics. However, this hypothesis remains speculative and necessitates further empirical study.

Eventually, the current state of the newly developed predictive approach remains preliminary due to lack of more data (and their associated cost). It is expected to be significantly refined as more data becomes available and at the same time assumptions are lifted, in particular as geochemical processes such as calcite dissolution and a potential influence of pH are incorporated into the models. In addition, fracture inclination and surface roughness could be incorporated into this framework with appropriate boundary layer assumptions.

Appendix A Non-dimensionalization of Navier-Stokes Momentum Balance

The momentum balance in the direction of gravity, including the Boussinesq approximation has the following form:

$$\begin{aligned}\rho_0 \frac{\partial v}{\partial t} + \rho_0 \left(\frac{\partial uv}{\partial x} + \frac{\partial vv}{\partial y} + \frac{\partial wv}{\partial z} \right) \\ = -\frac{\partial p + \rho_0 g y}{\partial y} + \mu \left(\frac{\partial^2 v}{\partial x^2} + \frac{\partial^2 v}{\partial y^2} + \frac{\partial^2 v}{\partial z^2} \right) + \rho_0 g \gamma \Delta x_{\mathrm{CO_2}}\end{aligned} \tag{A1}$$

A standard way, using the approach that a dimensional quantity can be described with a characteristic dimensional quantity and a dimensionless quantity (similiar to Section 2.3), to non-dimensionalize yields:

$$\begin{aligned}\frac{\rho_0 v_c}{t_c} \left(\frac{\partial \widehat{v}}{\partial \widehat{t}} \right) + \frac{\rho_0 u_c^2}{L_c} \left(\frac{\partial \widehat{u}\widehat{v}}{\partial \widehat{x}} + \frac{\partial \widehat{v}\widehat{v}}{\partial \widehat{y}} + \frac{\partial \widehat{w}\widehat{v}}{\partial \widehat{z}} \right) \\ = -\frac{p_c}{L_c} \frac{\partial \widehat{p}}{\partial \widehat{y}} + \frac{\mu v_c}{L_c^2} \left(\frac{\partial^2 \widehat{v}}{\partial \widehat{x}^2} + \frac{\partial^2 \widehat{v}}{\partial \widehat{y}^2} + \frac{\partial^2 \widehat{v}}{\partial \widehat{z}^2} \right) + \rho_0 g \gamma \Delta x_{\mathrm{CO_2},c} \widehat{x}_{CO_2}\end{aligned} \tag{A2}$$

Choosing $t_c = \frac{L_c}{v_c}$ and $p_c = \rho_0 v_c^2$ and then dividing by $\frac{\rho_0 v_c^2}{L_c}$ yields:

$$\begin{aligned}\frac{\partial \widehat{v}}{\partial \widehat{t}} + \frac{\partial \widehat{u}\widehat{v}}{\partial \widehat{x}} + \frac{\partial \widehat{v}\widehat{v}}{\partial \widehat{y}} + \frac{\partial \widehat{w}\widehat{v}}{\partial \widehat{z}} \\ = \frac{\partial \widehat{p}}{\partial \widehat{y}} + \frac{\mu}{\rho_0 v_c L_c} \left(\frac{\partial^2 \widehat{v}}{\partial \widehat{x}^2} + \frac{\partial^2 \widehat{v}}{\partial \widehat{y}^2} + \frac{\partial^2 \widehat{v}}{\partial \widehat{z}^2} \right) + \frac{\rho_0 g \gamma \Delta x_{\mathrm{CO_2},c} L_c}{\rho_0 v_c^2} \widehat{x}_{CO_2}\end{aligned} \tag{A3}$$

Appendix B Numerical Settings

Aperture	Cell No. x [-]	Cell No. y [-]	Cell No. z [-]	Cell Width x [m]	Cell Width y [m]	Cell Width z [m]	Max. Aspect Ratio
1 mm	700	10	1400	2.86×10^{-04}	1.0×10^{-04}	2.86×10^{-04}	2.86
1 cm	400	20	800	5.0×10^{-04}	5.0×10^{-04}	5.0×10^{-04}	1.0
10 cm	200	100	400	1.0×10^{-03}	1.0×10^{-03}	1.0×10^{-03}	1.0

Table B1: Summary of meshes used in the simulations.

Finite Volume Shemes	
Gradient Scheme	Gauss linear
Divergence Scheme	Gauss upwind
Laplacian Scheme	Gauss linear uncorrected
Interpolation Scheme	linear

Table B2: Summary of Finite-Volume schemes used in the simulations.

Linear Solver Settings					
Equation	Solver	Preconditioner	Smoother	Tolerance	Relative Tolerance
p	GAMG		DIC	1×10^{-06}	1×10^{-02}
U	PBiCGStab	DILU		1×10^{-08}	1×10^{-03}
CO_2	PBiCGStab	DILU		1×10^{-06}	1×10^{-04}

Table B3: Summary of linear solvers used in the simulations.

Appendix C Derivation of Dimensional and Dimensionless Flux (Efficiency)

C1 Dimensional

Raw data from the custom OpenFOAM solver consists of the global sum of concentration times the cell volume for each time step. Multiplying this by the molar volume yields the moles in the system at a given time.

$$n_{\mathrm{CO_2}} = \sum_{i=0}^{n_{cell}} x_{\mathrm{CO_2},i} \times \rho_{mol,i} \times V_i \ [\mathrm{mol}] \tag{C1}$$

However, the quantity of interest is the amount of moles crossing the interface per unit of time. Assuming that ρ_{mol} remains constant over time, this yields for the change of

moles over time:

$$\dot{n}_{\mathrm{CO_2}} = \frac{\Delta n_{\mathrm{CO_2}}}{\Delta t} \text{ [mol/s]} \tag{C2}$$

The mole flux over the interface is therefore:

$$\dot{n}_{\mathrm{CO_2}}\big|_{Interface} = \frac{\dot{n}_{\mathrm{CO_2}}}{A_{Interface}} \text{ [mol/m}^2\text{ s]} \tag{C3}$$

C2 Dimensionless

For the analysis of dimensionless quantities we start again at eq. (C1).
First, we introduce the dimensionless molar amount.

$$\hat{n}_{\mathrm{CO_2}} = \frac{n_{\mathrm{CO_2}}}{x_{\mathrm{CO_2},c} \times \rho_{mol} \times V_{fracture}} \text{ [–]} \tag{C4}$$

The dimensionless time is now scaled using a characteristic velocity and the fractures depth :

$$\hat{t} = \frac{t \times u_c}{d} \text{ [–]} \tag{C5}$$

Characteristic flux yields:

$$\dot{\hat{n}}_{\mathrm{CO_2}} = \frac{\Delta \hat{n}_{\mathrm{CO_2}}}{\Delta \hat{t}} \text{ [–]} \tag{C6}$$

The relationship between eq. (C3) and eq. (C6) is:

$$\dot{n}_{\mathrm{CO_2}}\big|_{Interface} = \dot{\hat{n}}_{\mathrm{CO_2}} \times x_{\mathrm{CO_2},c} \times \rho_{mol} \times u_c \tag{C7}$$

Rearranging yields:

$$\frac{\dot{n}_{\mathrm{CO_2}}\big|_{Interface}}{x_{\mathrm{CO_2},c} \times \rho_{mol} \times u_c} = \dot{\hat{n}}_{\mathrm{CO_2}} = \langle F \rangle \tag{C8}$$

This relationship highlights the interpretation that the dimensionless flux can be seen as a measure of flux efficiency.

Appendix D Analysis of Characteristic Velocities for Multiple Control Heights

As seen in Figure 1, breakthrough curves are determined at various heights. For the exemplary fracture of height 0.4 m, these heights are at 38, 35, 30, 25, 5 cm, respectively. Breakthrough times are now evaluated by comparing the average concentration at a given height to a threshold of 1×10^{-06} times the boundary concentration. The difference in time and distance is then equated to a finger-front velocity. Due to the close proximity of the 38 cm control height and a premature detection of fingering due to diffusion, the velocities are only determined using the layers below.

The effect of a non-constant characteristic velocity is depicted in Figures D1 and D2. Note that due to the discrete nature of our control heights the curves do overlap but their magnitude remains farily similar.

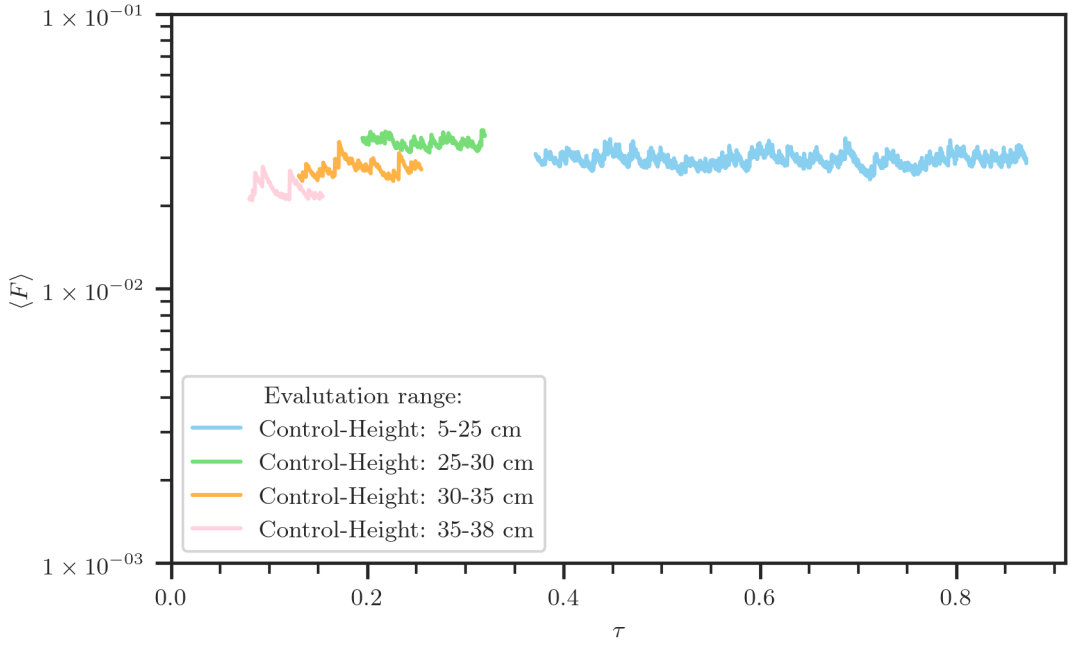

Figure D1: Flux efficiency against dimensionless time for a fracture of aperture 1 mm and a concentration of 1×10^{-04} mol/mol at the boundary. The overlapping is caused by the scaling of τ which includes in our case a depth and time dependent characteristic velocity u_c.

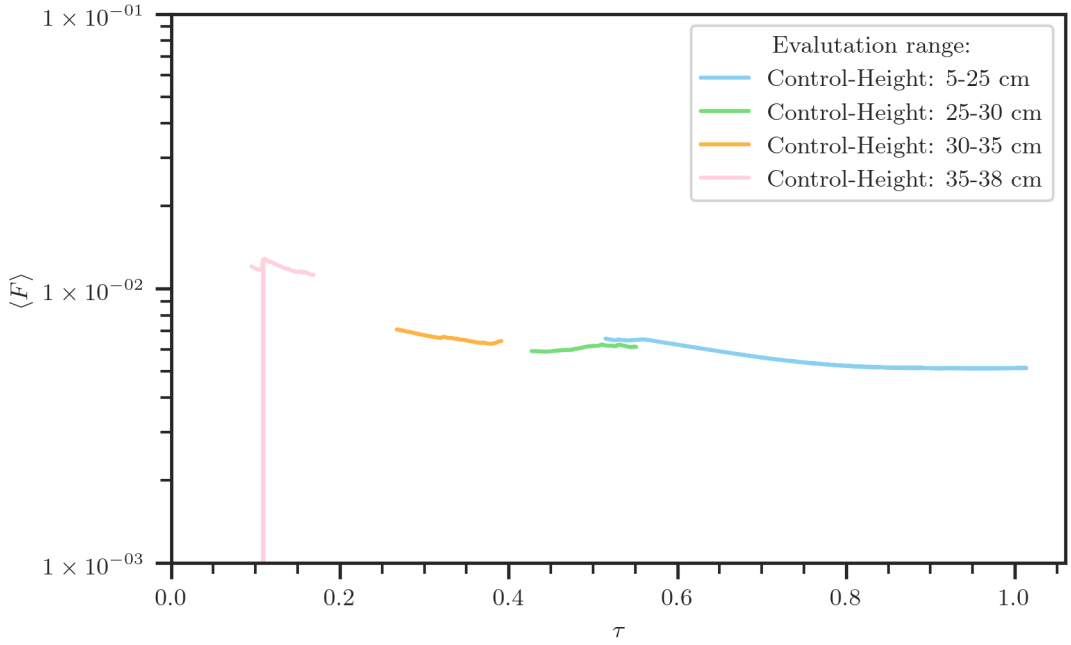

Figure D2: Flux efficiency against dimensionless time for a fracture of aperture 1 mm and a concentration of 1×10^{-04} mol/mol at the boundary. The overlapping is caused by the scaling of τ which includes in our case a depth and time dependent characteristic velocity u_c.

Appendix E Definition and Usage of the Critical Rayleigh Number

From the chosen approach that

$$\langle F \rangle = \frac{1}{\lambda_{\langle F \rangle} Ra} + \langle F \rangle_\infty \tag{E1}$$

by defining $\langle F \rangle_{const.} \equiv 1.2 \langle F \rangle_\infty$ we obtain the critical Rayleigh number:

$$Ra_{crit} = \frac{1}{0.2 \lambda_{\langle F \rangle} \langle F \rangle_\infty} \tag{E2}$$

Furthermore in (Figure 8) it was found that:

$$\lambda_{\langle F \rangle} = \frac{\langle F \rangle_\infty + 0.9685}{48.299} \tag{E3}$$

Inserting leads to:

$$Ra_{crit} = \frac{48.299}{0.2 \langle F \rangle_\infty (\langle F \rangle_\infty + 0.9685)} \tag{E4}$$

For the line, seperating the Rayleigh invariant part in Figure 7, the functional relationship of the form $\langle F \rangle_{const.} = f(Ra)$ is of interest. Rearranging with $\langle F \rangle_\infty = \langle F \rangle_{const.}/1.2$, wo obtain :

$$\langle F \rangle_\infty (\langle F \rangle_\infty + 0.9685) = \frac{48.299}{0.2 Ra_{crit}} \tag{E5}$$

Solving this quadratic formula and choosing the additive solution:

$$\langle F \rangle_\infty = -\frac{0.9685}{2} + \sqrt{\frac{0.9685^2}{2} + \frac{48.299}{0.2 Ra_{crit}}} \tag{E6}$$

Finally:

$$\langle F \rangle_{const.} = -1.2 \left(\frac{0.9685}{2} + \sqrt{\frac{0.9685}{2}^2 + \frac{48.299}{0.2 Ra_{crit}}} \right) = \langle F \rangle \tag{E7}$$

E1 Derived Characteristic Velocity and Characteristic Height

Once a critical Rayleigh number is known, characteristic velocity and characteristic height are still unknown. From the definition of Ra and the presvious investigations, it is proposed that Ra_{crit} is:

$$Ra_{crit} = \frac{u_c \chi_c}{D} \tag{E8}$$

Using the Schmidt number one can define a criterion for the derivative of $a^\star$:

$$Re_\chi = Ra_{crit}/Sc = \frac{u_c \chi_c}{\nu} \tag{E9}$$

Using boundary-layer theory and Equations (22) and (E8) results in a system of equations:

$$0 = Ra_{crit} - \frac{u_c \chi_c}{D} \tag{E10}$$

$$0 = \begin{cases} 0 - \frac{-5}{\frac{u_c \chi_c}{\nu}^{1/2}} & \text{for } a \leq 2\delta \\ \frac{-5}{Re_\chi{}^{1/2}} - \frac{-5}{\frac{u_c \chi_c}{\nu}^{1/2}}, & \text{for } a > 2\delta \end{cases} \tag{E11}$$

The system can be solved using, for example, a least squares algorithm with an initial guess of u and χ such that $a > 2\delta$.

Open Research Section

The code used in the simulation is available as source code and pre-compiled in a Docker image in Keim and Class (2024a). Furthermore, scripts for post-processing the results are available in Keim and Class (2024b).

Acknowledgments

Funded by Deutsche Forschungsgemeinschaft (DFG, German Research Foundation) under Germany's Excellence Strategy - EXC 2075 – 390740016. We acknowledge the support by the Stuttgart Center for Simulation Science (SimTech). The work is further associated (without receiving funding) with Project C04 of the Collaborative Research Center 1313 (Project Number 327154368 – SFB 1313, German Research Foundation, DFG).

References

Ahlers, G., Grossmann, S., & Lohse, D. (2009, April). Heat transfer and large scale dynamics in turbulent Rayleigh-Bénard convection. *Reviews of Modern Physics*, *81*(2), 503–537. doi: 10.1103/RevModPhys.81.503

Ahlers, G., & Xu, X. (2001, April). Prandtl-Number Dependence of Heat Transport in Turbulent Rayleigh-Bénard Convection. *Physical Review Letters*, *86*(15), 3320–3323. doi: 10.1103/PhysRevLett.86.3320

Appelo, C. A. J., & Postma, D. (2010). *Geochemistry, groundwater and pollution* (2nd ed., 5th corr. repr ed.). Boca Raton: CRC Press.

Audra, P., & Palmer, A. N. (2011, December). The pattern of caves: Controls of epigenic speleogenesis. *Géomorphologie : relief, processus, environnement*, *17*(4), 359–378. doi: 10.4000/geomorphologie.9571

Bachu, S., Bonijoly, D., Bradshaw, J., Burruss, R., Holloway, S., Christensen, N. P., & Mathiassen, O. M. (2007, October). CO2 storage capacity estimation:

Methodology and gaps. *International Journal of Greenhouse Gas Control*, *1*(4), 430–443. doi: 10.1016/S1750-5836(07)00086-2

Bakalowicz, M. (2005, March). Karst groundwater: A challenge for new resources. *Hydrogeology Journal*, *13*(1), 148–160. doi: 10.1007/s10040-004-0402-9

Berre, I., Boon, W. M., Flemisch, B., Fumagalli, A., Gläser, D., Keilegavlen, E., ... Zulian, P. (2021, January). Verification benchmarks for single-phase flow in three-dimensional fractured porous media. *Advances in Water Resources*, *147*, 103759. doi: 10.1016/j.advwatres.2020.103759

Bögli, A. (1980). *Karst Hydrology and Physical Speleology*. Berlin, Heidelberg: Springer Berlin Heidelberg. doi: 10.1007/978-3-642-67669-7

Boot-Handford, M. E., Abanades, J. C., Anthony, E. J., Blunt, M. J., Brandani, S., Mac Dowell, N., ... Fennell, P. S. (2014). Carbon capture and storage update. *Energy Environ. Sci.*, *7*(1), 130–189. doi: 10.1039/C3EE42350F

Class, H., Bürkle, P., Sauerborn, T., Trötschler, O., Strauch, B., & Zimmer, M. (2021, December). On the Role of Density-Driven Dissolution of CO $_2$ in Phreatic Karst Systems. *Water Resources Research*, *57*(12), e2021WR030912. doi: 10.1029/2021WR030912

Class, H., Ebigbo, A., Helmig, R., Dahle, H. K., Nordbotten, J. M., Celia, M. A., ... Wei, L. (2009, December). A benchmark study on problems related to CO2 storage in geologic formations: Summary and discussion of the results. *Computational Geosciences*, *13*(4), 409–434. doi: 10.1007/s10596-009-9146-x

Class, H., Keim, L., Schirmer, L., Strauch, B., Wendel, K., & Zimmer, M. (2023, February). Seasonal Dynamics of Gaseous CO2 Concentrations in a Karst Cave Correspond with Aqueous Concentrations in a Stagnant Water Column. *Geosciences*, *13*(2), 51. doi: 10.3390/geosciences13020051

Class, H., Weishaupt, K., & Trötschler, O. (2020, March). Experimental and Simulation Study on Validating a Numerical Model for CO2 Density-Driven Dissolution in Water. *Water*, *12*(3), 738. doi: 10.3390/w12030738

Covington, M. D. (2016, January). 8. The importance of advection for CO $_2$ dynamics in the karst critical zone: An approach from dimensional analysis. In *Geological Society of America Special Papers* (Vol. 516, pp. 113–127). Geological Society of America. doi: 10.1130/2015.2516(09)

De Paoli, M., Alipour, M., & Soldati, A. (2020, June). How non-Darcy effects influence scaling laws in Hele-Shaw convection experiments. *Journal of Fluid Mechanics*, *892*, A41. doi: 10.1017/jfm.2020.229

Dreybrodt, W. (1988). *Processes in Karst Systems* (Vol. 4; D. Barsch, I. Douglas, F. Joly, M. Marcus, & B. Messerli, Eds.). Berlin, Heidelberg: Springer Berlin Heidelberg. doi: 10.1007/978-3-642-83352-6

Duan, Z., & Sun, R. (2003, February). An improved model calculating CO2 solubility in pure water and aqueous NaCl solutions from 273 to 533 K and from 0 to 2000 bar. *Chemical Geology*, *193*(3-4), 257–271. doi: 10.1016/S0009-2541(02)00263-2

Elenius, M. T., & Johannsen, K. (2012, September). On the time scales of nonlinear instability in miscible displacement porous media flow. *Computational Geosciences*, *16*(4), 901–911. doi: 10.1007/s10596-012-9294-2

Ellis, B., Peters, C., Fitts, J., Bromhal, G., McIntyre, D., Warzinski, R., & Rosenbaum, E. (2011, September). Deterioration of a fractured carbonate caprock exposed to CO $_2$ -acidified brine flow. *Greenhouse Gases: Science and Technology*, *1*(3), 248–260. doi: 10.1002/ghg.25

Emami-Meybodi, H., Hassanzadeh, H., Green, C. P., & Ennis-King, J. (2015, September). Convective dissolution of CO2 in saline aquifers: Progress in modeling and experiments. *International Journal of Greenhouse Gas Control*, *40*, 238–266. doi: 10.1016/j.ijggc.2015.04.003

Ennis-King, J. (2005). Role of Convective Mixing in the Long-Term Storage of Carbon Dioxide in Deep Saline Formations. *SPE Journal*.

Fernø, M. A., Haugen, M., Eikehaug, K., Folkvord, O., Benali, B., Both, J. W., ... Nordbotten, J. M. (2023, September). Room-Scale CO2 Injections in a Physical Reservoir Model with Faults. *Transport in Porous Media*. doi: 10.1007/s11242-023-02013-4

Flemisch, B., Berre, I., Boon, W., Fumagalli, A., Schwenck, N., Scotti, A., ... Tatomir, A. (2018, January). Benchmarks for single-phase flow in fractured porous media. *Advances in Water Resources*, *111*, 239–258. doi: 10.1016/j.advwatres.2017.10.036

Flemisch, B., Nordbotten, J. M., Fernø, M., Juanes, R., Both, J. W., Class, H., ... Zhang, Z. (2023, August). The FluidFlower Validation Benchmark Study for the Storage of CO2. *Transport in Porous Media*. doi: 10.1007/s11242-023-01977-7

Gabrovšek, F., & Dreybrodt, W. (2000, May). Role of mixing corrosion in calcite-aggressive H_2O-CO_2-$CaCO_3$ solutions in the early evolution of Karst Aquifers in limestone. *Water Resources Research*, *36*(5), 1179–1188. doi: 10.1029/1999WR900337

Garcia, J. E. (2001, October). *Density of aqueous solutions of CO2* (Tech. Rep. Nos. LBNL–49023, 790022). doi: 10.2172/790022

Green, C., & Ennis-King, J. (2018, August). Steady Flux Regime During Convective Mixing in Three-Dimensional Heterogeneous Porous Media. *Fluids*, *3*(3), 58. doi: 10.3390/fluids3030058

Grossmann, S., & Lohse, D. (2000, March). Scaling in thermal convection: A unifying theory. *Journal of Fluid Mechanics*, *407*, 27–56. doi: 10.1017/S0022112099007545

Grossmann, S., & Lohse, D. (2001, April). Thermal Convection for Large Prandtl Numbers. *Physical Review Letters*, *86*(15), 3316–3319. doi: 10.1103/PhysRevLett.86.3316

Grossmann, S., & Lohse, D. (2004, December). Fluctuations in turbulent Rayleigh–Bénard convection: The role of plumes. *Physics of Fluids*, *16*(12), 4462–4472. doi: 10.1063/1.1807751

Hartmann, A., Goldscheider, N., Wagener, T., Lange, J., & Weiler, M. (2014, September). Karst water resources in a changing world: Review of hydrological modeling approaches. *Reviews of Geophysics*, *52*(3), 218–242. doi: 10.1002/2013RG000443

Hesse, M. A. (2008). Mathematical Modeling and Multiscale Simulation of CO2 Storage in Saline Aquifers.

Hidalgo, J. J., Fe, J., Cueto-Felgueroso, L., & Juanes, R. (2012, December). Scaling of Convective Mixing in Porous Media. *Physical Review Letters*, *109*(26), 264503. doi: 10.1103/PhysRevLett.109.264503

Hommel, J., Akyel, A., Frieling, Z., Phillips, A. J., Gerlach, R., Cunningham, A. B., & Class, H. (2020, June). A Numerical Model for Enzymatically Induced Calcium Carbonate Precipitation. *Applied Sciences*, *10*(13), 4538. doi: 10.3390/app10134538

Houillon, N., Lastennet, R., Denis, A., & Malaurent, P. (2020). The CO_2 dynamics in the continuum atmosphere-soil-epikarst and its impact on the karstification potential of water: A case study of the lasceaux cave site (montignac, france). In C. Bertrand, S. Denimal, M. Steinmann, & P. Renard (Eds.), *Eurokarst 2018, besancon - advances in the hydrogeology of karst and carbonate reservoirs* (pp. 93–99). Springer Nature Switzerland.

IAPWS Industrial Formulation 1997 for the Thermodynamic Properties of Water and Steam. (2008). In *International Steam Tables* (pp. 7–150). Berlin, Heidelberg: Springer Berlin Heidelberg. doi: 10.1007/978-3-540-74234-0_3

Iding, M., & Ringrose, P. (2010, March). Evaluating the impact of fractures on the performance of the In Salah CO2 storage site. *International Journal of Greenhouse Gas Control*, *4*(2), 242–248. doi: 10.1016/j.ijggc.2009.10.016

Ipcc. (2022). *Global Warming of 1.5° C: IPCC Special Report on Impacts of Global Warming of 1.5° C above Pre-industrial Levels in Context of Strengthening Response to Climate Change, Sustainable Development, and Efforts to Eradicate Poverty* (1st ed.). Cambridge University Press. doi: 10.1017/9781009157940

Kaufmann, G., Gabrovšek, F., & Romanov, D. (2014, June). Deep conduit flow in karst aquifers revisited. *Water Resources Research*, *50*(6), 4821–4836. doi: 10.1002/2014WR015314

Keim, L., & Class, H. (2024a). *Replication Code for: Rayleigh invariance allows the estimation of effective CO2 fluxes due to convective dissolution into water-filled fractures.* DaRUS. doi: 10.18419/darus-4089

Keim, L., & Class, H. (2024b). *Replication Data for: Rayleigh invariance allows the estimation of effective CO2 fluxes due to convective dissolution into water-filled fractures.* DaRUS. doi: 10.18419/darus-4143

Kelemen, P., Benson, S. M., Pilorgé, H., Psarras, P., & Wilcox, J. (2019, November). An Overview of the Status and Challenges of CO2 Storage in Minerals and Geological Formations. *Frontiers in Climate*, *1*, 9. doi: 10.3389/fclim.2019.00009

Kestin, J., Sokolov, M., & Wakeham, W. A. (1978, July). Viscosity of liquid water in the range -8 °C to 150 °C. *Journal of Physical and Chemical Reference Data*, *7*(3), 941–948. doi: 10.1063/1.555581

Klimchouk, A., Ford, D., Palmer, A., & Dreybrodt, W. (Eds.). (2000). *Speleogenesis - evolution of karst aquifers.* Huntsville Alabama: National Speleological Society.

Kneafsey, T. J., & Pruess, K. (2010, March). Laboratory Flow Experiments for Visualizing Carbon Dioxide-Induced, Density-Driven Brine Convection. *Transport in Porous Media*, *82*(1), 123–139. doi: 10.1007/s11242-009-9482-2

Kopp, A., Class, H., & Helmig, R. (2009, May). Investigations on CO2 storage capacity in saline aquifers—Part 2: Estimation of storage capacity coefficients. *International Journal of Greenhouse Gas Control*, *3*(3), 277–287. doi: 10.1016/j.ijggc.2008.10.001

Kukuljan, L., Gabrovšek, F., Covington, M. D., & Johnston, V. E. (2021, October). CO2 dynamics and heterogeneity in a cave atmosphere: Role of ventilation patterns and airflow pathways. *Theoretical and Applied Climatology*, *146*(1-2), 91–109. doi: 10.1007/s00704-021-03722-w

Lee, K. Y., Van Geldern, R., & Barth, J. A. (2021, July). Extreme gradients in CO2 losses downstream of karstic springs. *Science of The Total Environment*, *778*, 146099. doi: 10.1016/j.scitotenv.2021.146099

Letelier, J. A., Mujica, N., & Ortega, J. H. (2019, April). Perturbative corrections for the scaling of heat transport in a Hele-Shaw geometry and its application to geological vertical fractures. *Journal of Fluid Mechanics*, *864*, 746–767. doi: 10.1017/jfm.2019.3

Luetscher, M., & Jeannin, P.-Y. (2004, December). Temperature distribution in karst systems: The role of air and water fluxes. *Terra Nova*, *16*(6), 344–350. doi: 10.1111/j.1365-3121.2004.00572.x

March, R., Doster, F., & Geiger, S. (2018, March). Assessment of CO $_2$ Storage Potential in Naturally Fractured Reservoirs With Dual-Porosity Models. *Water Resources Research*, *54*(3), 1650–1668. doi: 10.1002/2017WR022159

Metz, B., & Intergovernmental Panel on Climate Change (Eds.). (2005). *IPCC special report on carbon dioxide capture and storage.* Cambridge: Cambridge University Press, for the Intergovernmental Panel on Climate Change.

Neufeld, J. A., Hesse, M. A., Riaz, A., Hallworth, M. A., Tchelepi, H. A., & Huppert, H. E. (2010, November). Convective dissolution of carbon dioxide in saline aquifers. *Geophysical Research Letters*, *37*(22), n/a-n/a. doi: 10.1029/2010GL044728

Nordbotten, J., Flemisch, B., Gasda, S., Nilsen, H., Fan, Y., Pickup, G., ...

Pruess, K. (2012, July). Uncertainties in practical simulation of CO2 storage. *International Journal of Greenhouse Gas Control*, *9*, 234–242. doi: 10.1016/j.ijggc.2012.03.007

Nordbotten, J. M., Boon, W. M., Fumagalli, A., & Keilegavlen, E. (2019, April). Unified approach to discretization of flow in fractured porous media. *Computational Geosciences*, *23*(2), 225–237. doi: 10.1007/s10596-018-9778-9

Omrani, S., Ghasemi, M., Mahmoodpour, S., Shafiei, A., & Rostami, B. (2022, January). Insights from molecular dynamics on CO2 diffusion coefficient in saline water over a wide range of temperatures, pressures, and salinity: CO2 geological storage implications. *Journal of Molecular Liquids*, *345*, 117868. doi: 10.1016/j.molliq.2021.117868

Pankow, James F. (2022). *Aquatic Chemistry Concepts*. S.l.: CRC PRESS.

Phillips, S., Igbene, A., Fair, J., Ozbek, H., & Tavana, M. (1981, June). *Technical databook for geothermal energy utilization* (Tech. Rep. Nos. LBL-12810, 6301274). doi: 10.2172/6301274

Riechelmann, S., Breitenbach, S., Schroder-Ritzrau, A., Mangini, A., & Immenhauser, A. (2019, June). Ventilation and cave air PCO2 in the Bunker-Emst Cave System (NW Germany): Implications for speleothem proxy data. *Journal of Cave and Karst Studies*, *81*(2), 98–112. doi: 10.4311/2018ES0110

Rutqvist, J., Birkholzer, J., & Tsang, C.-F. (2008, February). Coupled reservoir–geomechanical analysis of the potential for tensile and shear failure associated with CO2 injection in multilayered reservoir–caprock systems. *International Journal of Rock Mechanics and Mining Sciences*, *45*(2), 132–143. doi: 10.1016/j.ijrmms.2007.04.006

Scheer, D., Class, H., & Flemisch, B. (2021). *Subsurface Environmental Modelling Between Science and Policy*. Cham: Springer International Publishing. doi: 10.1007/978-3-030-51178-4

Song, J., & Zhang, D. (2013, January). Comprehensive Review of Caprock-Sealing Mechanisms for Geologic Carbon Sequestration. *Environmental Science & Technology*, *47*(1), 9–22. doi: 10.1021/es301610p

Unver, A. A., & Himmelblau, D. M. (1964). Diffusion Coefficients of CO2, C2H4, CsHe, and C4H8 in Water from 6° to 65° C. *Journal of Chemical and Engineering Data*, *9*(3).

Wagner, W., & Pruß, A. (2002, June). The IAPWS Formulation 1995 for the Thermodynamic Properties of Ordinary Water Substance for General and Scientific Use. *Journal of Physical and Chemical Reference Data*, *31*(2), 387–535. doi: 10.1063/1.1461829

White, J. A., Chiaramonte, L., Ezzedine, S., Foxall, W., Hao, Y., Ramirez, A., & McNab, W. (2014, June). Geomechanical behavior of the reservoir and caprock system at the In Salah CO $_2$ storage project. *Proceedings of the National Academy of Sciences*, *111*(24), 8747–8752. doi: 10.1073/pnas.1316465111

White, W. M. (2013). *Geochemistry*. Hoboken, NJ: John Wiley & Sons Inc.

Yan, W., Huang, S., & Stenby, E. H. (2011, November). Measurement and modeling of CO2 solubility in NaCl brine and CO2–saturated NaCl brine density. *International Journal of Greenhouse Gas Control*, *5*(6), 1460–1477. doi: 10.1016/j.ijggc.2011.08.004